

Improved numerical modelling of clusters of galaxies

Kampen, E. van

Citation

Kampen, E. van. (1995). Improved numerical modelling of clusters of galaxies. *Monthly Notices Of The Royal Astronomical Society*, 273, 295-327. Retrieved from https://hdl.handle.net/1887/6683

Version: Not Applicable (or Unknown)

License: Leiden University Non-exclusive license

Downloaded from: https://hdl.handle.net/1887/6683

Note: To cite this publication please use the final published version (if applicable).

Improved numerical modelling of clusters of galaxies

Eelco van Kampen*

Sterrewacht Leiden, Postbus 9513, 2300 RA Leiden, The Netherlands

Accepted 1994 September 15. Received 1994 June 16; in original form 1993 October 15

ABSTRACT

We have attempted to model the formation and evolution of clusters of galaxies consisting of both galaxy and dark background particles. Starting from initial conditions with only equal-mass dark particles, as traditionally done, at a certain epoch galaxies are identified using a local density percolation technique combined with a virial equilibrium condition. For each galaxy found, its constituent particles are replaced by a single softened particle, where the binding energy of the original particles is transferred into internal energy of the single particle galaxy. While rather crude, this is a first attempt to include dissipation (by hand) on galactic scales in inherently dissipationless N-body methods. More importantly, it keeps galaxies intact which would otherwise get disrupted within clusters because of either two-body or tidal effects. Not doing so results in smooth final mass distributions, in which galaxies cannot be identified, even for quite large particle numbers. The softening parameter of a galaxy is proportional to the half-mass radius of its original group, so a spectrum of masses and sizes is thus produced automatically. However, the softening of the dark background particles is still chosen on numerical grounds, since at present their nature and distribution are largely unknown.

These ideas have been tested on several matter distributions, including an average piece of universe, a small cluster (or group) of galaxies with a mass of around 2×10^{14} ${\rm M}_{\odot}$, regular clusters with a mass of almost 10^{15} ${\rm M}_{\odot}$, and a rich cluster heavier than 3×10^{15} ${\rm M}_{\odot}$. Galaxies are made 'instantly' at one or more redshifts, supposing a peak in the galaxy formation rate, with both a lower and an upper mass cut-off. The resulting mass functions compare reasonably to observed luminosity functions. Mass segregation of the galaxies with respect to the dark matter is shown to occur, with details depending on the epoch of galaxy formation. A clear spatial bias between these two mass components is observed. There is only marginal evidence for velocity bias in some of the simulations. The segregation and biasing effects cause a general underestimation of the total cluster mass. $H_0 = 50 \ {\rm km \ s^{-1} Mpc^{-1}}$ is adopted throughout the paper.

Key words: methods: numerical – galaxies: clusters: general – galaxies: formation – galaxies: luminosity function, mass function – dark matter – large-scale structure of Universe.

1 INTRODUCTION

Clusters of galaxies are the most massive self-gravitating single objects presently known to exist in our Universe, and are therefore of major interest to cosmology. Large catalogues of observed clusters of galaxies exist. This makes it possible to study the variations in their global properties which can in turn be used to test theories of formation and evolution of the large-scale structure of the Universe. However, only the luminous component has been mapped reasonably well, especially in the optical (e.g. Abell 1958; Dickey 1988), radio (e.g.

O'Dea & Uson 1986), and X-ray wavelengths (e.g. Forman & Jones 1982; Sarazin 1986). Most of this radiation, except for the X-rays, is related to the galaxies. To understand the observational properties of clusters of galaxies we need to model the formation of their member galaxies. We will not deal here with the intrinsic properties of these galaxies, but will study their distribution in cluster phase-space, their mass spectrum and how well they trace the total mass distribution, focusing on issues like mass segregation, spatial bias and velocity bias.

Modelling of clusters of galaxies is an intrinsically nonlinear problem, and therefore numerical methods are most often used. The standard N-body method uses N equally massive particles which sample the mass distribution of the cluster and its immediate environment. Aarseth (1963) was the first to apply this method to clusters, and, although there was far

^{*} Present address: Royal Observatory Edinburgh, Blackford Hill, Edinburgh EH9 3HJ, evk@roe.ac.uk

less computer power at the time, it was a vast improvement over analytical calculations. Over the years faster computers became available, so higher resolution experiments became feasible (e.g. White 1976; Turner et al. 1979; McGlynn 1984; Frenk et al. 1990, and many others), and cluster models could be devised for several cosmological scenarios (e.g. West, Dekel & Oemler 1989; van Haarlem & van de Weygaert 1993). Several approaches to improve the modelling further include the addition of smoothed particle hydrodynamics (SPH) to incorporate dissipational effects (e.g. Evrard 1990; Katz & White 1993; Evrard, Summers & Davis 1994), the use of many more particles to increase the resolution (e.g. Carlberg 1994), and the inclusion of many physical effects operating on galactic scales in a parametrized form (e.g. Mamon 1987).

With the aim of producing a large model catalogue in mind, we limit ourselves to relatively modest particle numbers and gravitational interaction only, but we do include a method to make galaxies 'by hand' in order to ensure their survival. At a certain epoch, groups of simulation particles found to represent a galaxy will be replaced by single particles, thereby assuming that after that epoch galaxies can be treated as single entities. It will be demonstrated that this is really necessary, because galaxies, or rather dark haloes, which form during the cluster evolution are easily disrupted in standard N-body models. This is either a result of two-body disruption, which is a numerical artefact, or due to tidal disruption, a real physical effect

To form the galaxies, we use a local density percolation technique supplemented with a virial equilibrium condition. The galaxies thus found are modelled by a single softened particle, and the remaining matter is considered dark. The choice for the softening of the dark matter before and after the galaxy formation step is important for its general evolution, but also influences the galaxy formation process. The dark matter should be softened according to its nature, but the type and amount of softening will still be based on numerical considerations because the nature of the dark matter is as yet largely unknown.

In Section 2 we describe the simulation sets used and their purpose, demonstrate the problem of galaxy disruption, and present the solution along with the precise methods chosen. Choices for the parameters are discussed and tested in Section 3. This includes the softening for both the galaxy and the dark matter particles, and two ad hoc parameters in the galaxy formation recipe. In Section 4 we test the galaxy formation method for several formation epochs in order to study the influence of the epoch of galaxy formation on the properties of the resulting clusters. Section 5 gives the first quantitative results on some global properties of the model clusters built.

2 GALAXIES IN N-BODY CLUSTER MODELS

2.1 The simulation set

We first describe the five sets of simulations used in this paper, and their specific purpose. Each set, of which the overall properties are listed in Table 1, consists of several simulations which have just one parameter varying. The background model for all simulations is an Einstein-de Sitter unbiased cold dark matter (CDM) universe. The Hubble parameter H_0 is usually given in a dimensionless form as $H_0 = 100h_0^{-1}$ km s⁻¹Mpc⁻¹.

Because the CDM spectrum has a characteristic length which scales as $\Omega_0^{-1}h_0^{-2}$, while observed sizes of objects scale as h_0^{-1} , to change h_0 changes the physical model. We therefore chose to remove the h_0 scaling and adopt a value of 50 km s⁻¹Mpc⁻¹ for H_0 , i.e. $h_0 = \frac{1}{2}$.

The main motivation for using N-body simulations is that the non-linear evolution of the density distribution can be followed more realistically. But equally important in any model building is to start from the right initial conditions in the most practical way. For this purpose we use a constrained random field method as first developed by Bertschinger (1987). He used an iterative and approximate approach, which was later improved upon by Hoffman & Ribak (1991) who solved the problem exactly. With this method one can constrain a Gaussian random field to form a specified 'object' at a certain point in space. In fact, one can put more than one constraint on the field, restricting the properties of one object or specifying various objects. Clearly, the more constraints one imposes, the less probable the resulting object will be. The theory of Gaussian random fields enables us to calculate the corresponding probability densities (e.g. Bardeen et al. 1986).

As the name suggests, the constrained random field method is restricted to cosmological scenarios that assume structure to form from gravitational instabilities in an initial Gaussian-distributed density fluctuation field. Proto-objects in the initial density field $\delta(\mathbf{r})$ are defined as peaks (or dips) in its smoothed counterpart $\delta^W(\mathbf{r})$, obtained by convolving $\delta(\mathbf{r})$ with a Gaussian window function

$$W(r) = (2\pi R_{\rm S}^2)^{-\frac{3}{2}} e^{-r^2/2R_{\rm S}^2} . {1}$$

So each object is defined by the smoothing scale $R_{\rm S}$ and its density excess δ^W . Constraints are most conveniently expressed in units that characterize the expected values of the quantities constrained. Root-mean-square values for the smoothed density field and derived (linear) functions, which depend on the cosmological scenario through the power spectrum, are most suitable for this purpose. Define a set of spectral moments for a density field smoothed with a Gaussian filter of width $R_{\rm S}$ (Bardeen et al. 1986):

$$\sigma_j^2(R_{\rm S}) \equiv \int \frac{k^2}{2\pi^2} |\delta_k|^2 e^{-R_{\rm S}^2 k^2} k^{2j} dk , \qquad (2)$$

where δ_k is the Fourier transform of the unsmoothed density field and $|\delta_k|^2$ its power spectrum. With this definition $\sigma_0(R_S)$ is the rms density fluctuation of the smoothed field δ^W , and we can express amplitude constraints as $v\sigma_0(R_S)$ peaks (or dips).

Specification of only $\delta^W = \nu \sigma_0(R_S)$ requires just one constraint. This initial amplitude is assumed to be the value calculated backwards from the present to the initial epoch assuming linear evolution. This will in general not be correct for significant overdensities, since non-linear evolution will produce a larger final amplitude, and one has to iterate a few times to obtain the correct initial amplitude. We can specify the object further by the first and second spatial derivatives of δ^W (at the same point). We always set the gradient $\nabla \delta^W$ equal to zero to be certain of a local extremum. This accounts for three extra constraints. The second derivative tensor $\nabla_i \nabla_j \delta^W$ has six independent quantities, resulting in six additional constraints. They define the shape (two constraints), the orientation (three constraints) and the size (one constraint) of the object. The latter

Table 1. Parameters of the basic simulation sets and resulting main cluster properties. A value of 50 km s⁻¹ Mpc⁻¹ is adopted for H_0 .

sim. set	constraint	R _s [Mpc]		size [Mpc]	$\langle n \rangle$ [Mpc ⁻³]	$r_{\rm nn}^P$ [Mpc]	ϵ [Mpc]	$m_{ m part}$ $[10^{10}{ m M}_{\odot}]$	R _{turn} [Mpc]	$\begin{array}{c} M_{turn} \\ [10^{15} M_{\odot}] \end{array}$	M_{Abell} [$10^{15}M_{\odot}$]
A	none	_	16672	20.0	0.51	0.39	var.	1.7	-	-	_
В	$3\sigma_0$ peak	4.0	19042	20.0	0.51	0.39	var.	1.7	6	0.3	0.2
C	$2\sigma_0$ broad peak	8.0	18125	40.0	4.1	0.78	var.	14	11	1.4	0.8
D	$2\sigma_0$ broad peak	8.0	146654	40.0	0.51	0.39	0.02	1.7	11	1.6	0.7
E	$5\sigma_0$ peak	8.0	143641	80.0	4.1	0.78	0.05	14	20	12.0	3

is usually defined in a dimensionless form as the curvature

$$x \equiv -\frac{\nabla^2 \delta^W}{\sigma_2(R_{\rm S})} \,, \tag{3}$$

which is positive for a peak, and negative for a dip.

The simulations of set A represent an average piece of universe within a sphere of radius 20 Mpc, giving a reference frame for the other simulations containing overdensities. For set B we chose a small cluster in order to study the effects of softening in a not too violent environment but with power on small scales. The initial conditions for sets A and B were generated using an implementation of Bertschinger's method which can constrain δ^W at the centre of the simulation volume for any cosmological density fluctuation spectrum (van de Weygaert 1991; van de Weygaert & van Kampen 1993). Only set B has a constraint in fact: a $3\sigma_0$ peak for 4-Mpc Gaussian smoothing. This corresponds to a total mass of $\approx 2 \times 10^{14} M_{\odot}$ within the Abell radius of 3 Mpc (Abell 1958). An example of the outcome of one of its simulations is shown in Fig. 1. Set B can be considered a group or poor cluster, of which Fornax or Dorado would be examples (Ferguson & Sandage 1990).

An implementation of the Hoffman-Ribak method (van Haarlem & van de Weygaert 1993; van de Weygaert & Bertschinger 1994) became available to us after performing the simulations of sets A and B. We utilized its abilities to build a somewhat extended, not too rich cluster, which will remain isolated during most of the evolution, and does not collapse too rapidly. This is simulation set C. The amplitude of the 8-Mpc Gaussian smoothed density field in the centre of the simulation sphere is set to 2σ , and the three gradients are set to zero. The smoothing scale is twice that taken for sets A and B. The 2σ amplitude is chosen to prevent many clusters forming nearby, since higher peaks cluster more strongly. Finally the 6 independent second derivatives were given values such that the peak will be broad enough to prevent a fast collapse of the peak. A value of 1 was taken for the curvature x, while ≈ 2 is the expectation value according to Gaussian random field theory (Bardeen et al. 1986). These constraints do not produce a typical cluster; we deliberately selected a quiet, isolated cluster to test the ideas presented. The top row of Fig. 13 displays four stages of the evolution of one of the models of set C. Test set D is similar to set C, but at higher resolution. We took 8 times more particles in the same volume and applied the same constraints as in set C, but with a different random number seed yielding a different realization. The main purpose of these simulations is to test resolution issues. The particle distributions at z = 2 and at the present epoch are shown in Fig. 2. The models from both sets C and D are comparable to, for example, Virgo A (Binggeli, Tammann & Sandage 1987).

Finally, we examine an example of a very rich cluster of the well-observed Abell type: the target objects of our method. A 5σ peak for 8-Mpc Gaussian smoothing with zero gradients gives such a very rich cluster, comprising set E. The second derivatives were chosen such that the cluster has a typical shape and extent; a triaxial shape with axial ratios 1:1.31:1.56 was taken, while we set the mean curvature x to 4.2. Both choices have the highest probability (Bardeen et al. 1986). We should note here that these numbers are valid for linear evolution only, so different final values will result. For a large peak of this size, the simulation sphere has to be large enough to encompass all the matter that will end up in the cluster at the present epoch. The boxsize was therefore taken to be twice as large as for sets C and D. To retain the same resolution as for set C, the number of particles was increased accordingly. An observed counterpart of this model might be Abell 1069 from the sample of Beers et al. (1991). Their sample consists solely of double clusters, which set E turns out to be also (Section 5).

2.2 Identifying galaxies: local density percolation

In order to compare N-body cluster models to observations we need to find the galaxies, i.e. physical groups of particles, in these models. A frequently used algorithm to identify groups in a distribution of particles is percolation, also called friends-of-friends. This links all particles together with a pairwise separation less than a certain cut-off length. Velocity information is not used in this method, and the local density is not taken into account either. The latter omission is in fact a major defect of the ordinary percolation method, because the local density strongly influences the kind of groups found. It will not separate substructure within large haloes, but does link together strangely shaped groups in lowdensity regions. This is demonstrated clearly by Bertschinger & Gelb (1991). They solve this problem by a method called DENMAX which temporarily evolves all bound particles in a quasi-hydrodynamical fashion to examine which particles will end up in a real halo when dissipation is taken into account. This produces very good results, but requires a substantial amount of CPU-time in practice. Because our final goal is a large catalogue of models we have to be keen on performance, so we chose to improve upon the plain percolation method by actually using the local density to determine a local percolation length. Particles should be linked together when they are

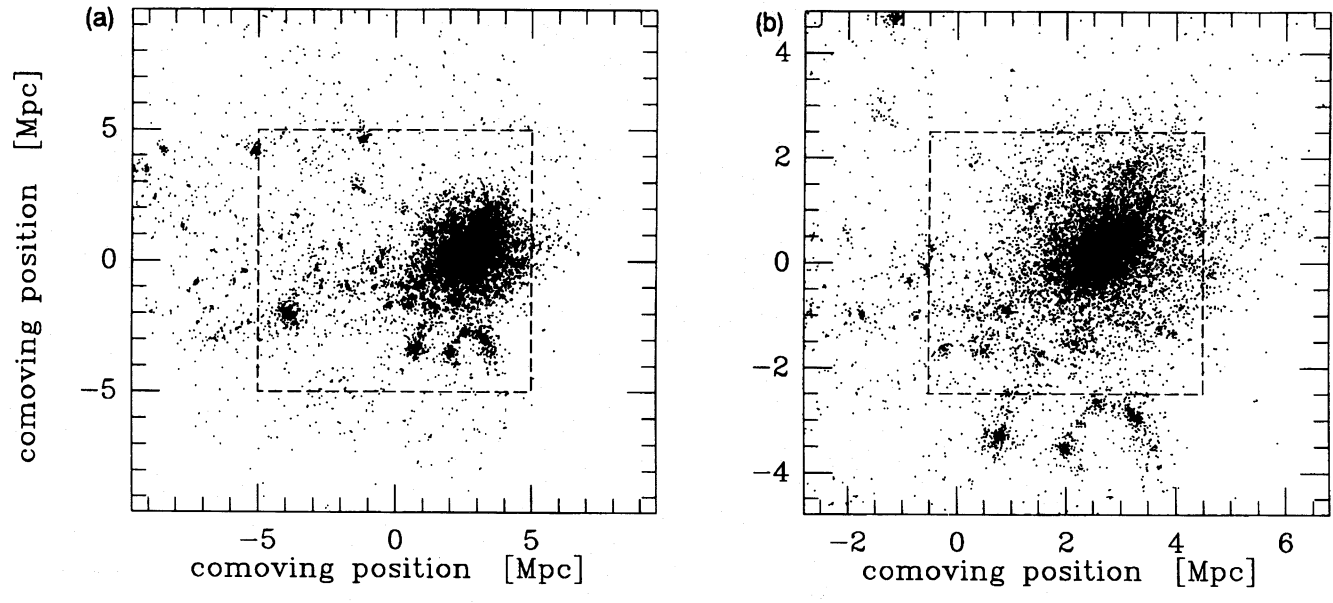


Figure 1. Example of the outcome of a simulation from set B. The left panel shows the x - y projection of most of the simulation sphere; the right panel zooms in on the overdense region formed. The dashed lines indicate the region within which the power spectra shown in Fig. 5 were calculated.

separated by a distance less than a certain fraction of what is expected locally when the particles would be Poisson distributed. This idea resembles peak bias from a particle point of view.

A general particle distribution is clustered as described by the two-point correlation function $\xi(r)$. The average number of galaxies $\langle N \rangle$ within a radius r around a randomly chosen galaxy is given by

$$\langle N \rangle = \frac{4\pi}{3} r^3 \langle n \rangle + \frac{4\pi}{3} \langle n \rangle \int_0^r \xi(r') r'^2 dr' . \tag{4}$$

The average nearest neighbour distance r_{nn} is defined as the separation for which $\langle N \rangle = 1$. This is not easily derived from equation (4) for general $\xi(r)$. For a Poisson distribution ξ vanishes, and the Poissonian average nearest neighbour distance is therefore

$$r_{\rm nn}^{\rm P} \equiv [3/4\pi\langle n\rangle]^{1/3} \ . \tag{5}$$

The idea of local density percolation is to use the *local* number density instead of its global average, so for this purpose we define the Gaussian smoothed number density field $n^W(r, R_S)$, being the number density field n(r) convolved with the Gaussian window function (1). This introduces the Gaussian smoothing length R_S as a free parameter of the method. We will use it in a dimensionless form, and express it in units of r_{nn}^P :

$$s \equiv R_{\rm S}/r_{\rm nn}^{\rm P} \ . \tag{6}$$

The local percolation length then is a fraction p of r_{nn}^{P} which is modulated according to the local density:

$$R_p(\mathbf{r},s) = p \ r_{\rm nn}^{\rm P} \left[\frac{n^W(\mathbf{r},s)}{\langle n \rangle} \right]^{-1/3} . \tag{7}$$

This defines the fraction p as the second free parameter of our method. A problem with (7) is that the local density is different for each particle tested, and therefore so is R_p . The simplest

way out is to take the mean of the two local percolation lengths for each pair. Another problem arises in low-density regions. We need to prevent groups from forming too easily in these regions, where R_p would become very large. So we should adopt a maximum for R_p , since slight overdensities in underdense regions are not expected to collapse within a Hubble time. A first choice for this maximum would be $r_{\rm nn}^{\rm P}$, the local percolation length corresponding to the mean number density, arriving at

$$R_p(\mathbf{r}_{ij}) = p\left(\frac{6}{\pi}\right)^{\frac{1}{3}} \operatorname{Min}\left\{ (n_i^W)^{-\frac{1}{3}} + (n_j^W)^{-\frac{1}{3}}, 2\langle n \rangle^{-\frac{1}{3}} \right\}, \tag{8}$$

where we used (5) to simplify the expression. This is similar to a recently published adaptive-linking method by Suto, Cen & Ostriker (1992) and Suginohara & Suto (1992, hereafter SuSu), although they use a different maximum length, which is r_{nn} for a totally anti-correlated distribution (all particles on a grid). More importantly, they use an absolute maximum, i.e. their maximum length is not multiplied by the percolation parameter p, as done in (8). These differences are most prominent in regions of average density: our method is of a more global nature while the adaptive-linking method by Suto et al. (1992) and SuSu is somewhat biased towards overdense regions. Before starting the local density percolation algorithm, we selected only locally bound particles, i.e. particles with a negative comoving binding energy, because unbound particles are expected to leave the local region and should therefore not be grouped into bound systems like galaxies.

After geometrically grouping particles together we want to make sure that these groups resemble physical galaxies. In general these are systems in virial equilibrium, and have half-mass radii satisfying

$$R_{\rm h} \approx 0.4 \frac{GM}{\sigma^2} \tag{9}$$

(Spitzer 1969). This is also true for the Plummer and Hernquist

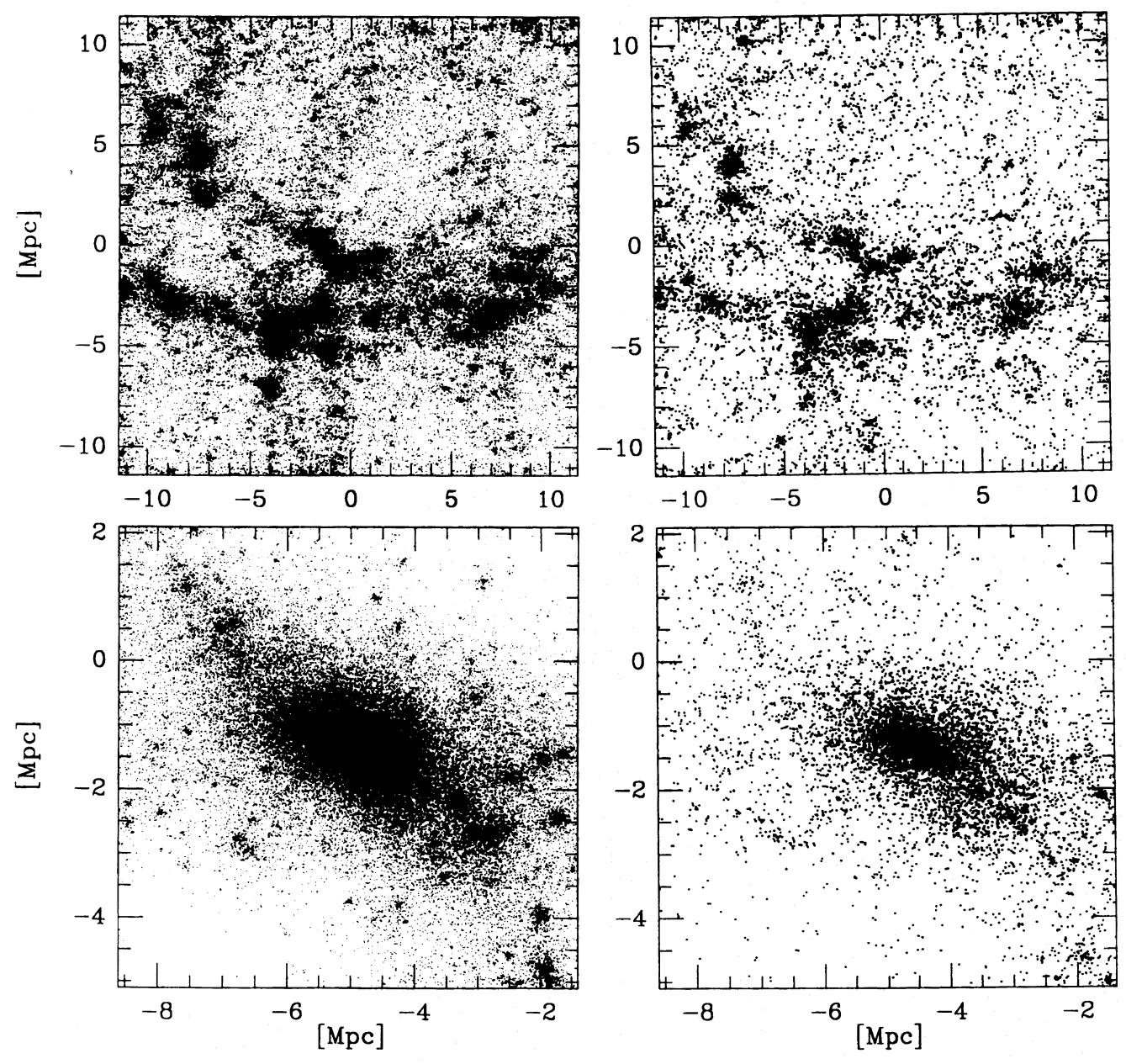


Figure 2. x - y projections of part of the volume of the high-resolution simulation D1 (left column) and its low-resolution counterpart D2 (right column) at z=2 (top row) and z=0 (bottom row).

profiles (see Appendix B) used extensively in this paper. We apply this relation as a second criterion for whether a galaxy has formed: only groups for which condition (9) is satisfied within a factor of two are considered to be galaxies. This latter freedom has to be allowed because of the numerical noise for groups consisting of a small number of particles, but also because the virial theorem does not really apply for a system of softened particles: one should use the Clausius Virial instead (equation (24), discussed in Section 3.3). Also, since the softening of the original individual particles influences the structure of the group, this determines the size of the formed galaxy as well. This is the reason for the margin in applying condition (9), where the lower factor of two is in fact the mass for which the group is marginally bound.

2.3 Disruption of galaxies in traditional cluster modelling

The cluster member galaxies are modelled by at most a few hundred particles each, instead of the $\approx 10^{10}$ stars in real systems. Even the largest simulations to date (e.g. Gelb 1992) have 'only' a few thousand particles per galaxy. This gives rise to the question whether this introduces undesired discreteness effects. Traditionally one just evolves a distribution of equal-mass particles and identifies 'galaxies' at the present epoch, letting the N-body integrator sort out their formation and evolution by itself. These 'galaxies' are in fact dark haloes, since all types of matter are modelled and the haloes are by far the dominant component. In the following we will call the whole system of a dark halo contain-

ing a spiral/elliptical galaxy, either with or without gas, a 'galaxy'.

Use of a standard N-body method may seem the best approach, but there are significant problems when simulating a cluster of galaxies, even with a very large number of particles. Simulation set D demonstrates this: galaxies are identified at z=2 using the method presented in Section 2.2, after which we investigate what happens to them during the cluster formation. In order to make visualization possible, we select 39 haloes with masses in the range $0.9 - 1.1 \times 10^{12} \text{ M}_{\odot}$, as identified at z = 2. The left cube of the top row of Fig. 3 shows the positions of the particles in those haloes (the full distribution at that epoch is plotted in the upper left panel of Fig. 2). The right cube of Fig. 3 displays the final distribution of the same particles, demonstrating the disruption of many of the groups identified at z = 2, mostly those within the main cluster (shown fully in the bottom left panel of Fig. 2). We will argue in the next two subsections that this disruption is due to either numerical two-body effects or (physical) tidal disruption.

2.3.1 Two-body disruption

Small N-body groups suffer from relatively fast two-body relaxation and might therefore evaporate. The time-scale of evaporation is usually about a hundred times larger than the relaxation time-scale (Binney & Tremaine 1987, page 526), but can be shorter than a Hubble time for very small N. This type of relaxation can be suppressed by softening: this property is in fact the major reason for using it, along with the desire to preserve the collisionless nature of the dark matter being modelled. However, softening also prevents groups becoming bound tightly on the softening scale, since soft interaction potentials increase the total energy of the group, enhancing evaporation again. This effect is similar to 'soft-core evaporation', which prevents the formation of compact cores in any N-body group consisting of soft particles.

Two-body relaxation by itself is not sufficient for the fast disruption we observe for groups crossing the main cluster. Still, the disruption might be explained by two-body effects, with the main difference that the relaxation time should no longer be governed by the properties of the groups itself, but by the surrounding cluster. The 'cold' group relaxes towards the 'hot' cluster conditions, heating up so much that the group no longer remains bound, and diffuses into the cluster system. We will first estimate the time-scale for this two-body disruption process, and then compare it to the tidal disruption time-scale.

First consider a group in the field outside the cluster. Such an isolated N-body system has a relaxation time t_r which is usually expressed in units of the crossing time $t_c \equiv R/v$, where R is the size of the system and v the rms velocity of its member particles. So we have $t_r \equiv n_r t_c$, where n_r is the number of crossing times it takes for average velocity changes $\langle \Delta v \rangle$ due to interactions to become of the order of the average velocity v within the group. Relaxation is usually defined in terms of the velocities squared:

$$n_{\rm r} \equiv \frac{v^2}{\langle \Delta v \rangle^2} \ . \tag{10}$$

For a system that is already roughly in equilibrium one can deduce (e.g. Binney & Tremaine 1987):

$$\langle \Delta v \rangle^2 \approx 8 \left(\frac{Gm}{Rv}\right)^2 N \ln \Lambda ,$$
 (11)

where $\ln \Lambda \equiv \ln(b_{\rm max}/b_{\rm min})$ is the Coulomb logarithm, which contains the ratio of maximum and minimum impact parameters b. For $b_{\rm max}$ one usually takes the size R of the system (see however Smith 1992). Because of the use of softened potentials $b_{\rm min}$ is mostly determined by the softening scale ϵ . Farouki & Salpeter (1982) found empirically that $b_{\rm min} \approx 4\epsilon$ if it is larger than the point particle value $b_{\rm min} \equiv Gm/v^2$. For a point mass system we can derive that $\Lambda \approx N$ (e.g. Binney & Tremaine 1987), so we take $\Lambda = \min\{N, R/4\epsilon\}$. Using (9) with $R \approx R_{\rm h}$, and the isotropy approximation $v^2 = 3\sigma^2$, we find

$$\langle \Delta v \rangle^2 \approx \frac{6}{N} v^2 \ln \Lambda \ .$$
 (12)

Substituting (12) in (10) we see that for the isolated group the v^2 terms cancel in the expression for n_r , and we find

$$t_{\rm r,ig} = \frac{N_{\rm ig}}{6 \ln \Lambda_{\rm ig}} t_{\rm c,ig} = \frac{N_{\rm ig} R_{\rm ig}}{6 v_{\rm ig} \ln \Lambda_{\rm ig}} , \qquad (13)$$

where the index 'ig' stands for 'isolated group'. Such a group will evaporate on a time-scale a hundred times larger (Binney & Tremaine 1987, page 491), so it dissolves on a time-scale

$$t_{\rm dis,ig} \approx 20 \frac{N_{\rm ig} R_{\rm ig}}{v_{\rm ig} \ln \Lambda_{\rm ig}} \ . \tag{14}$$

For typical galaxies in our simulation $N\approx10-50$, $R\approx20-50$ kpc, $v\approx200-300$ km s⁻¹, and $\Lambda\approx2$, and we find that $t_{\rm dis,ig}$ is about a Hubble time.

Consider now a group which has formed at some epoch and has relaxed to a state in which the particles move at a typical speed v_{ig} , i.e. for which the relaxation time is given by (13). When it falls into the cluster, where particles move at a typical speed v_{cl} , it will 'relax' towards the state of this cluster through two-body encounters. Finally the particles in the group will form part of the cluster and the group ceases to exist as a separate entity. For an estimate of the disruption time-scale, i.e. the time-scale of the particles relaxing to the cluster state, we keep v_{ig} in the numerator of (10), since if the internal kinetic energy is doubled the group will be genuinely disrupted. However, for the denominator of (10) we need to substitute (11) with v_{cl} , N_{cl} , N_{cl} , and $t_{r,cl}$. The disruption time-scale due to cluster particles is then

$$t_{\rm dis,cl} = \frac{v_{\rm ig}^2}{v_{\rm cl}^2} \frac{N_{\rm cl}}{6 \ln \Lambda_{\rm cl}} t_{\rm c,cl} . \tag{15}$$

Interestingly, because of the larger velocities of the cluster particles compared to the infalling group particles, equation (15) is more precise than equation (14) which applies to the group particles amongst themselves. In the derivation of (14) it is assumed that the perturbing particles travel on straight trajectories during encounters (see for example Binney & Tremaine (1987), chapter 4). This is best satisfied by the fast-moving cluster particles. Since $v_{\rm cl}$ will depend on the distance from the cluster centre, being largest in the centre, the disruption time will vary according to the orbit within the cluster, but an average value for $v_{\rm cl}$ still allows us to estimate typical disruption times. In order to compare $t_{\rm dis,cl}$ to $t_{\rm dis,ig}$ we need to measure in equal units of time. This amounts to replacing $t_{\rm c,cl}$ with $t_{\rm c,ig}$, leading to

$$t_{\text{dis,cl}} \equiv t_{\text{r,cl}} = \frac{v_{\text{ig}}^3}{v_{\text{cl}}^3} \frac{R_{\text{cl}}}{R_{\text{ig}}} \frac{N_{\text{cl}}}{6 \ln \Lambda_{\text{cl}}} t_{\text{c,ig}}$$

$$\approx \frac{v_{\text{cl}}}{v_{\text{ig}}} \frac{\rho_{\text{ig}}}{\rho_{\text{cl}}} \frac{N_{\text{ig}}}{6 \ln \Lambda_{\text{cl}}} t_{\text{c,ig}}.$$
(16)

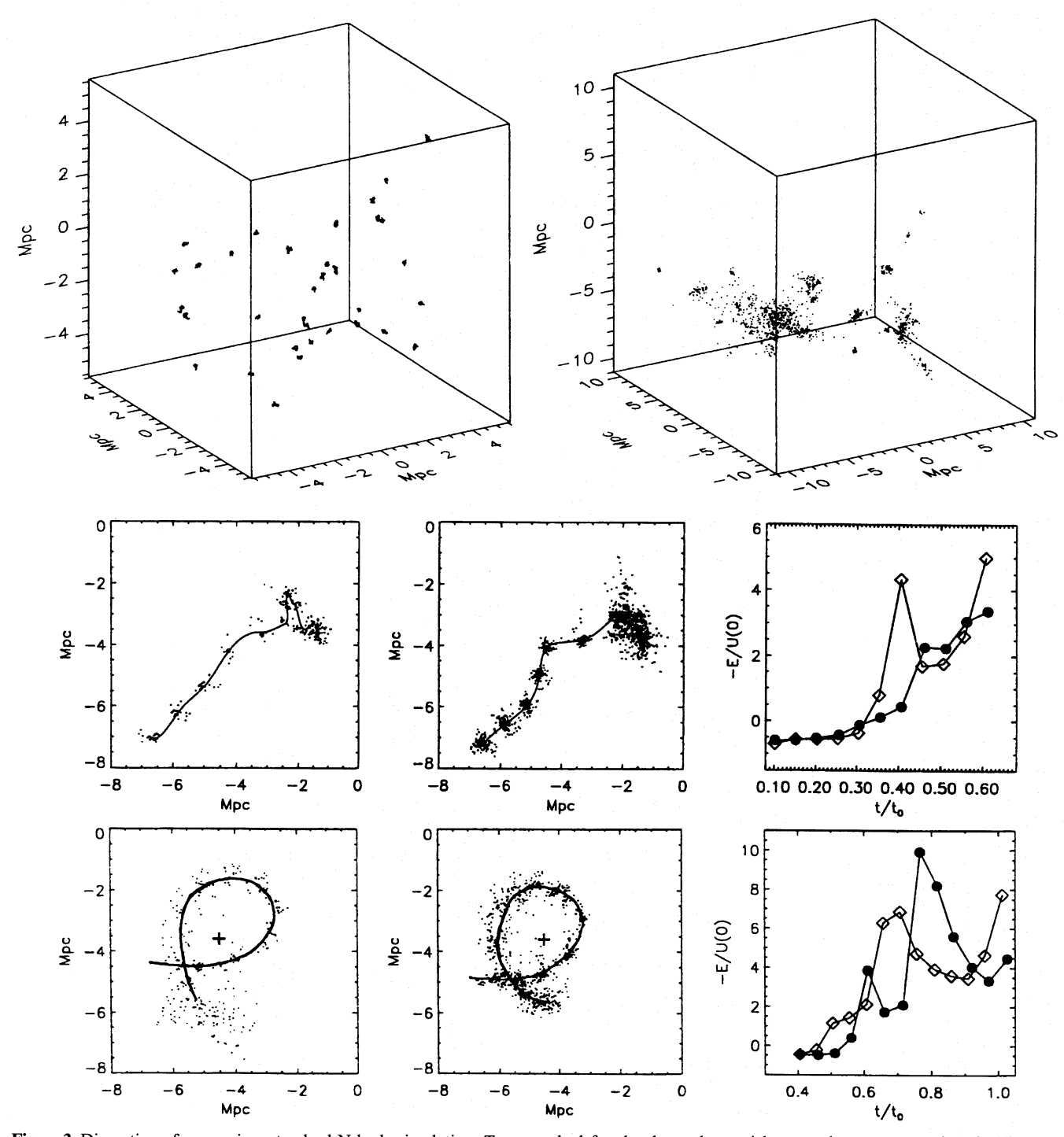


Figure 3. Disruption of groups in a standard N-body simulation. Top row: the left cube shows the particles tagged as group members in 39 groups with masses in the interval $0.9 - 1.1 \times 10^{12} \, \mathrm{M_\odot}$ using the local density percolation method at z=2 on the high-resolution simulation D1 (shown at the same epoch in the upper left panel of Fig. 2). The right cube shows the same particles at the current epoch, demonstrating that most of the groups were disrupted at the present epoch. Only groups that did not cross the main cluster survive. Middle row: example of the disruption of a group formed at z=4 in the high-resolution simulation (left) and in the low-resolution simulation (middle). The solid line shows the trajectory, the cross indicates the centre of the cluster at the present epoch. The right panel shows the internal binding energy in units of the initial internal potential energy of the group for the low-resolution run (open symbols) and high-resolution one (closed). The difference in gradients at $t/t_0 \approx 0.4$, when the group enters the forming cluster, indicates that two-body encounters with the cluster particles drive the disruption of the group. Bottom row: as in the middle row, but for a group formed at z=1 that travels around the main cluster. In this case tidal forces dominate the disruption.

For the last substitution we used that $\rho \sim N/R^3$ by definition and that $v^2 \sim N/R$ for an isotropic system roughly in virial equilibrium. Comparing this time-scale to the disruption

time-scale (14) for an isolated group, we find a ratio

$$\frac{t_{\rm dis,ig}}{t_{\rm dis,cl}} = 100 \frac{v_{\rm cl}^3}{v_{\rm ig}^3} \frac{N_{\rm ig}}{N_{\rm cl}} \frac{R_{\rm ig}}{R_{\rm cl}} \frac{\ln \Lambda_{\rm cl}}{\ln \Lambda_{\rm ig}} \approx 100 \frac{v_{\rm ig}}{v_{\rm cl}} \frac{\rho_{\rm cl}}{\rho_{\rm ig}} \frac{\ln \Lambda_{\rm cl}}{\ln \Lambda_{\rm ig}}$$
(17)

between the two. For a typical group within a typical cluster this ratio is about 3, with $v_{\rm cl}\approx 1500~{\rm km~s^{-1}}, v_{\rm ig}\approx 300~{\rm km~s^{-1}}, N_{\rm cl}/N_{\rm ig}\approx 300, R_{\rm cl}/R_{\rm ig}\approx 50,$ and $\Lambda_{\rm cl}/\Lambda_{\rm ig}\approx 2.$

The main point is that, although the relaxation time due to cluster particles is much longer (a factor of 20 in our configuration) than that due to fellow group particles, the lifetime of a group is still shorter when it resides in a cluster. This is because the evaporation time of isolated groups is about a hundred times $t_{r,ig}$, while the disruption time of such groups within a cluster is equal to $t_{r,cl}$. The interactions with 'hot' cluster particles always increase the velocities of the 'cold' group particles, while the diffusion process underlying evaporation both increases and decreases velocities, so each particle first has to reach the high-velocity tail of the Maxwell distribution before it can leave the group.

Since $t_{\rm dis,ig}$ is about a Hubble time, an average group falling into a cluster disrupts in about a third of a Hubble time. Therefore at least some of the groups formed at z=2 that subsequently fell into the cluster are likely to be disrupted by two-body interactions with the cluster particles. For our simulations we have $R\approx 4$ Mpc and N larger than a few thousand, so Λ always depends on ϵ roughly as $\sim 1/\epsilon$. This can only enlarge the disruption time by a factor of three for our largest sensible choice for the softening parameter, $\epsilon=50$ kpc. To take more particles lengthens the disruption timescale only by a factor $N/\ln N$. This is also true in the case of softening since more particles need a smaller choice for ϵ , changing like $N^{-1/3}$, so $\ln \Lambda$ is proportional (but not equal) to $\ln N$.

In a related paper, Huang, Dubinski & Carlberg (1993) claim that relaxation in softened systems is linearly proportional to N. However, this is based on taking a constant softening parameter while varying N over a large range. Therefore their claim is correct, but a constant ϵ causes strong overlapping of particle profiles for large N, especially for the rather large value for ϵ they took for their tests. This makes their models difficult to apply to physical systems. We expect that for smaller ϵ they would have observed a transition from an $N/\ln N$ dependence for small and intermediate N towards a linear scaling for large N.

In an impressive one million particle cluster simulation Carlberg (1994) also notices disruption of his galaxies, and blames this mainly on the two-body disruption process. His expression for the two-body disruption time-scale, for which he does not give a derivation, is a factor 16/6 smaller than (15). Carlberg's models have about the same size as ours and use $\epsilon=7.8$ kpc, so his $\ln\Lambda\approx 6$. Because of the higher resolution his galaxies survive somewhat longer, but the inner 500 kpc of his cluster contains only one identifiable galaxy.

2.3.2 Tidal disruption

We argued that the disruption of galaxies which traverse clusters in N-body simulations might be caused by two-body disruption, which is a numerical artefact. But we also know that galaxies within clusters must be limited to some maximum size because of the mean tidal field. Tidal forces can also disrupt a galaxy completely if its internal energy is doubled. In the simplest approximation of point masses with the galaxy in circular orbit at a distance R from the cluster centre, the

tidal radius is given by

$$r_{\rm tid} \approx R \left[\frac{M_{\rm gal}(r_{\rm tid})}{M_{\rm cl}(R)} \right]^{1/3}$$
 (18)

Tidal forces will be strongest where the potential gradient is largest. This will be somewhere near the half-mass radius, were the cluster has $M(R) \sim R$, i.e. $M(R) = MR/R_h$. The tidal radius will not be very small, and, because dark haloes have $M(r) \sim r$ as well, we find

$$r_{\rm tid} \approx R \sqrt{\frac{R_{\rm h} M_{\rm gal}}{r_{\rm h} M_{\rm cl}}}$$
 (19)

Typically $R_h/r_h \approx 30$ and $M_{\rm gal}/M_{\rm cl} \sim N_{\rm gal}/N_{\rm cl} \approx 1/300$, so the tidal radius is about a third of the distance of the galaxy to the cluster centre.

In reality most orbits are not circular and the cluster mass distribution is extended, which increases the tidal radius somewhat (Saslaw 1985, chapter 51). Taking this into account, Allen & Richstone (1988) found that even the largest galaxies will not be tidally truncated in a typical cluster potential. On the contrary, Merritt (1988) derives significantly smaller tidal radii. He argues that on the one hand at least part of the dark halo of a galaxy can be stripped during a cluster crossing without influencing the luminous component, but that on the other hand some fraction of the haloes will be destroyed, adding mass to the cluster halo and/or the central dominant galaxy. Both possibilities are there, and the likelihood of either one depends on a rather large number of parameters including the form of the orbits, the phase-space distribution of both the galaxies and the cluster dark matter, and the amount of dynamical friction. The latter brings galaxies into the 'danger zone', a broad shell around the cluster core where tidal forces are strongest. Like numerical two-body disruption, tidal disruption is able to destroy a galactic halo completely, depending on its ability to restore itself after a core-crossing. Galaxies can also be partly destroyed and lose orbital energy (Heisler & White 1990), bringing them towards the very centre of the cluster.

So we have the difficulty that both the two-body and the tidal disruptions have the same net effect and are strongest near the cluster core. Therefore we expect that the one that dominates will always be at least enhanced by the other: tidal forces decrease the density of a group, which shortens the twobody disruption time-scale (16), while two-body interactions puff up the group, which increases its size and makes it more liable to tidal forces. However, we can discriminate between the two by examining different resolutions, because the numerical disruption depends on the number of particles, while tidal disruption is independent of resolution. Therefore we compare the high-resolution simulation D1 with its low-resolution counterpart D2 in order to establish whether a difference in disruption time-scales between the simulations exists. The lowresolution simulation D2 is obtained by filtering simulation D1 with a simple, triangular shaped filter function. One-eighth of the particles thus remain. The distributions of both simulations D1 and D2 at z = 2, as well as a close-up of the end results at z = 0, were shown in Fig. 2. The disruption itself was demonstrated in Fig. 3 (top row). We examine several groups that formed at various redshifts, and which are initially well isolated and identifiable for both resolutions. We find that many of the groups that get near or into the cluster can easily get disrupted within a Hubble time due to either or both of the disruption processes. We illustrate this with two extreme examples, where the first one is destroyed mainly by two-body disruption, while the second one is disrupted by the tidal field of the cluster.

The first example is a group that was identified at a redshift of 4. The time evolution of the particles in that group is shown for both resolutions in the middle row of Fig. 3. It is destroyed at about the same time in both models after it falls into the forming cluster. In the right panel of the middle row of Fig. 3 we plot the internal binding energy of the two groups (in units of the initial internal potential energy) as a function of time. The open symbols represent the lowresolution run, the filled circles the high-resolution one. The gradient of the curve is then roughly inversely proportional to the disruption time-scale. For this group we see that the low-resolution group disrupts faster than the high-resolution one, indicating that two-body interactions are the driving force here. We monitored the component of the force on the particles of the group directed inwards to the centre of the group, and indeed found that for this group the tidal forces were generally too small to cause the disruption. The second example we look at is a group formed at z = 1 that does not fall into the main cluster, but travels at a more or less circular orbit around it. This is the optimal trajectory for tidal disruption, and we see from monitoring the forces that tidal forces are now strong enough to cause the observed damage to the group. The same type of plots as for the first group are shown in the bottom row of Fig. 3. The disruption time-scales seem to be roughly equal, although both plots of the internal binding energy as a function of time are quite noisy.

2.4 Incorporating galaxy formation in N-body cluster models

The observed disruption of galaxies in standard N-body simulations of clusters makes these types of simulations unsuitable for cluster modelling. Galaxy formation is probably a dissipational process, resulting in more tightly bound groups as compared to a purely gravitational collapse. Such groups are more difficult to break up. Probably only part of the galaxy is made up of baryonic matter, so dissipational effects should not be overestimated, but we should certainly not underestimate them: even while it is only the baryonic matter that will dissipate, this will still deepen the potential well, causing the non-baryonic matter to close in as well. Numerical codes using gravitational interactions only are intrinsically dissipationless. Furthermore, the need to use soft particles weakens the binding of the group. To preserve the member galaxies during the cluster evolution without the use of numerical hydrodynamics (which does that quite well, e.g. Evrard et al. 1994, but requires much CPU time and has many problems of its own), a group of particles which can be identified as a (proto-)galaxy at some epoch will in the simulations be replaced by a single soft particle with the properties of the original group. The amount of energy dissipated this way can be linked to the internal kinetic and potential energy of the galaxy formed. Remember, we only transform a group found by local density percolation into a single particle galaxy when the system is roughly in virial equilibrium, i.e. when condition (9) is satisfied to within a factor of two.

The position of the new galaxy is simply the centre-ofmass of the group of particles, and its velocity the massweighted mean of the velocities. This conserves momentum, but not energy. Because the velocities are vector summed, the kinetic energy of the new particle will be less than the sum of the kinetic energies of the original particles. Therefore the new density configuration, one large soft particle instead of a collection of smaller soft particles, will have a different potential energy. The choice of the softening parameter will determine the potential energy of the galaxy formed, and because of energy conservation also the amount of internal kinetic energy of the galaxy, which can be stored in both radial motion and rotation, and/or be put into the formation of stars and the heating of gas. It is obvious that there is a lot of freedom in redistributing the energy. Since the exact physics is difficult to model on galactic scales in a cluster-scale simulation, we have to make simplifying assumptions. Note that the exact size of the galaxy is not the most important issue here: for distant encounters it is irrelevant, while close encounters cannot be modelled very precisely anyway because we are forced to use rather large integration timesteps. It is merely that we need to keep the galaxies intact, and have their sizes roughly right.

We choose to make the actual distribution of particles within groups determine the amount of softening for the newly formed galaxy particle by taking the value of ϵ that corresponds to the half-mass radius of the group as given by (B8) for Plummer softening or by (B14) for Hernquist softening. This produces a spectrum of galaxy sizes. The galaxy particles are then evolved to the present epoch along with the remaining loose particles which form the background dark matter distribution. This means that mergers and tidal effects are not incorporated, which is an important approximation in the current modelling. Mergers can be dealt with, either by using a separate merging criterion, or by applying the galaxy formation algorithm several times during the evolution. The latter is glanced at in Section 4.4. Tidal stripping is taken into account to the extent that not all particles in the outer parts of haloes are included in the group by the local density percolation algorithm, and can thus be stripped during the evolution after the galaxy formation step. This clearly depends on the choice of the galaxy formation parameters p and s. An important implication of tidal stripping, which will occur for at least a fraction of the cluster members, is that the galaxies will lose orbital energy and sink to the cluster centre (Heisler & White 1990).

2.5 Resolution issues

To examine the influence of resolution on our galaxy formation method, we globally compare the high-resolution simulation D1 with its equivalent low-resolution run D2. We first look at the high-resolution simulation D1. Due to the larger number of particles we see many small clumps forming at z=2, most of which do not survive the formation of the main cluster. In the low-resolution simulation D2, many groups form at z=2 as well, but arguably in a noisier fashion. The final distribution is of course more discrete than that of D1, but the shape of the main cluster is not too different, and some of the surrounding groups can be identified in D1 as well.

Can we identify groups at z=2 equally well in both low- and high-resolution simulations? Scatter diagrams of M against $2.5R_h\sigma^2/G$ for both D1 and D2 are used to answer this (see Fig. 4). The high-resolution run D1 performs just a little better with the group parameters closely following the virial

304 E. van Kampen

line (equation 9), but the low-resolution simulation performs still quite well. This must be due to the smaller degree of clustering at this epoch, reflected in the far better correspondence of the particle distribution at z=2 as compared to the present epoch (see Fig. 2). At the high-mass end there are about 10 groups with masses above $10^{13} \, \mathrm{M}_{\odot}$ for both D1 and D2, with a slight difference in their mass spectra, mainly due to shot noise for D2. Differences in the distribution of group properties will grow at later times, but are still reasonably small at z=2. We conclude that resolution effects are less severe at high and medium redshifts than at the present epoch.

3 SOFTENING AND GALAXY FORMATION PARAMETERS

Before testing the actual galaxy formation method we will discuss the best possible choices for the parameters involved. The type and amount of softening are treated first, since these also influence the galaxy formation process. Up to now, potential softening has only been used for numerical reasons. It reduces two-body relaxation effects, preserves the collisionless nature of the dominating dark matter component, and enables the use of larger integration timesteps because small-scale potential fluctuations are suppressed. Normally one chooses the type of softening and its scale such that the numerical code performs well, but it would be more desirable to put some observables and physics in this choice. Galaxies form during the evolution of a cluster, introducing some degree of discreteness to the system. This should not be artificially reduced by excessive softening.

In our models we represent galaxies by single 'soft' particles, i.e. particles with a density profile. For these galaxy particles we should choose the type of softening and its scale such that the softening density profile resembles typical galactic halo density profiles as closely as possible. Besides the *Plummer* type of softening, which is mainly chosen because it behaves well numerically, we will also consider *Hernquist* softening, which might be a better model for the galaxy particles while being computationally convenient as well. A summary of the properties of both types of softening is given in Appendix B.

Softening (mostly of the Plummer type) has been used either in the coexpanding form, i.e. a constant multiplied by the expansion factor a (amongst many others: Efstathiou et al. 1985; Bertschinger & Gelb 1991; SuSu), or in the constant form (e.g. Hernquist 1987). Even a combination of the two. motivated by changing clustering properties in different stages of the evolution, is adopted in a recent paper by Warren et al. (1992). The reason for using coexpanding softening is simply that many N-body codes use coexpanding variables, in which the Layzer-Irvine cosmic energy equation remains valid only if the shape of the softened force-law remains fixed in coexpanding coordinates. This does not imply that the total physical energy is conserved. In fact, energy is lost and put into the soft particles which have an internal potential energy inversely proportional to $\epsilon(t)$ (equations (B11) and (B16)). We will use the coexpanding softening only for comparison with other work. One should further note that in calculations utilizing the PM or P³M methods (Hockney & Eastwood 1981) the softening is necessarily coexpanding due to the nature of the numerical method. Use of the treecode or the direct sum approach (e.g. Aarseth 1963) allows one to retain the freedom of the softening time dependence.

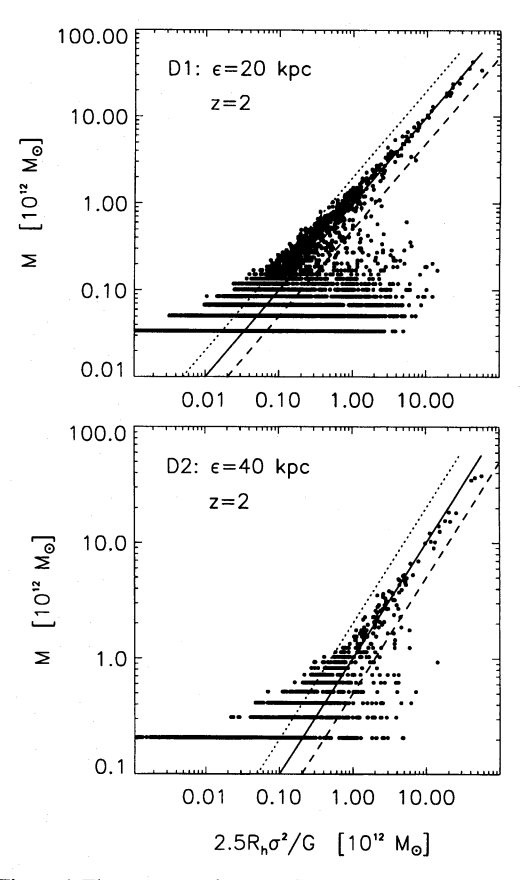


Figure 4. The mass M of groups found by the local density percolation technique as a function of $2.5R_h\sigma^2/G$ at z=2 for simulations D1 (top) and D2 (bottom), the latter being the low-resolution version of the first.

3.1 The softening parameter for background particles

Generally most of the simulation particles sample the invisible (dark) matter distribution, which is very likely to be the dominant mass component in clusters (e.g. Fitchett 1990). The choice for the softening of these particles should be determined by the nature of the cluster dark matter. However, since its nature is largely unknown, a choice on numerical grounds might still be the best option. Different choices for ϵ have been shown to produce different results with respect to properties of dark matter haloes (Warren et al. 1992) and group relaxation times (Farouki & Salpeter 1982; Smith 1992), so this matter deserves some attention here.

3.1.1 Numerical limits

At the start of an N-body simulation all particles are slightly displaced from their initial positions on a lattice using the Zel'dovich approximation. At that time the softening should be less than the spacing of the lattice to prevent strong overlapping of the density profiles, so ϵ therefore depends on the number of particles and the physical size of the simulation. Use of *coexpanding* softening removes the second dependence, and only the initial grid spacing remains to be considered. A value of at most one fifth of the spacing is often taken (e.g. Efstathiou et al. 1985, where one should note that their parameter $\eta \approx 2.4\epsilon$). If clustering is not rapid the particles will form

a Poisson distribution first (because the grid configuration is anti-correlated and therefore energetically unfavourable), otherwise they will tend to cluster immediately as described by the correlation function $\xi(r,t)$. In the first case the average nearest neighbour distance for any galaxy is just $r_{\rm nn}^{\rm P}$, as given by (5). For the case of rapid clustering we have to solve (4) using the evolving clustering statistic $\xi(r,t)$. This latter case is applicable to most of the cluster evolution, and should therefore be used to get an upper limit on the softening parameter ϵ .

The lower limit on ϵ is constrained numerically by the global integration timestep during interactions and the desire to keep the code as collisionless as possible, i.e. deflections during close encounters should be minimal. Approximate limiting criteria derived for these two issues are given in Appendix A. The best thing to do is to use the first criterion (equation A4) to constrain the timestep for a choice of ϵ , which should preferably be larger than the 'maximum scatter' value approximated by the second criterion (equation A2), and see if the experiment is still feasible given the computer time resources.

3.1.2 Clustering of equal-mass soft particles

In order to study the influence of the choice of softening, several sets of simulations were run from exactly identical initial conditions, but with a range of choices for the softening parameter ϵ for the two types of softening, differing by factors of 5. This comprises the test sets A, B, and C. The values for ϵ for set C were twice those of A and B because the size of the simulation sphere of set C is twice as large. We added two $\epsilon = 100$ kpc simulations (A8 and B8) and an $\epsilon = 200$ kpc simulation (C4) to compare with three corresponding Hernquist runs, as described below. Furthermore, both constant and coexpanding parameters were tested for the two types of softening. Since Hernquist softening has harder potentials, it is expected to suffer most from numerical problems at early times when $\epsilon'a(t)$ is really small. Finally, simulations C5 and C6 were added to compare to large-scale simulations which usually need to adopt a somewhat large softening parameter.

For the analysis we obtained the two-point correlation function $\xi(r)$ for all simulations. It is calculated by counting pairs within a certain sphere within the simulation volume, and comparing these with pair counts for a Poissonian distribution in the same sphere. The two-point correlation function is then given by

$$\xi(x) = \frac{\text{\#data pairs}(x)}{\text{\#Poisson pairs}(x)} q^2 \Delta^2 - 1 , \qquad (20)$$

where Δ is the local density contrast within the sphere and q is the ratio between the number of Poisson points and the number of data points. A larger q minimizes the noise in the determination of $\xi(r)$ but increases the computation time, so it can be used to compromise between the two. We will investigate the two-point function itself in Section 5; here we just use it to calculate average nearest neighbour distances (by integrating (4) numerically). These are needed to test criterion (A4) for the integration timestep, but they are also useful as a global indication of the amount of clustering. The rms peculiar velocity of the particles is calculated as well, which is also needed for the timestep criterion. All computed numbers are listed in Tables 2(a) and 2(b) for Plummer and Hernquist softening respectively, along with the predicted maximum integration timestep for the choice f = 1/4 in (A4). We also list the

energy conservation numbers, quantifying how well the simulation performed numerically. Note that in the simulations the timestep is less than or equal to $0.1 \times \Delta t_0$ (as described in Appendix A), while Δt_0 itself is listed in Table 2. The minimum softening based on the maximal scatter criterion (A2) is about 10 kpc for set A, 2 kpc for set B and 1 kpc for set C. We allow a maximum change of 10 per cent in $\Delta v/v$ from individual encounters. Note that for set A the number of interactions will be less than for sets B and C, since no cluster forms.

The most direct diagnostic for the amount of clustering on various scales is the power spectrum $|\delta_k^2|$ of the density fluctuation field $\delta(x)$, where δ_k is the Fourier transform of $\delta(x)$. The root-mean-square density fluctuation is given by $\delta_{\rm rms} \equiv \langle \delta^2(x) \rangle^{1/2}$. The contribution to $\delta_{\rm rms}$ from a logarithmic interval in k is

$$\delta_{\rm rms}(k) \approx \left(\frac{4\pi}{V}\right)^{1/2} k^{3/2} |\delta_k| \ .$$
 (21)

This is what is usually plotted to show the power on a certain mass scale, since $\delta_{\rm rms}(k)$ is proportional to $\delta M/M$, the *rms* mass fluctuation. To obtain power spectra for our simulated clusters we first sample the density distribution on a grid (i,j,k):

$$\rho_{ijk} = \sum_{n} W(|\mathbf{r}_n - \mathbf{r}_{ijk}|) . \tag{22}$$

The mass assignment function W(r) is chosen to be a Gaussian with a width of one cell. In fact one applies small-scale smoothing in order to remove shot noise present in a discrete particle distribution. The Fast Fourier Transform of the sampled data cube is calculated and divided by the Fourier Transform of W(r), to correct for the effects of the initial small-scale smoothing. Binning of the absolute wave numbers gives the square root of the power spectrum, $|\delta_k|$, from which $\delta_{\rm rms}(k)$ is calculated using (21).

3.1.3 Plummer softening

Looking at the results of the Plummer runs as collected in Table 2(a), it is clear that a large coexpanding softening parameter causes a considerable gain of energy, up to 13 per cent. However, most of the energy gained is due to this coexpansion. Adjustment of the softening parameter will change all pair interaction potentials and thus the total potential energy of the system. This is best seen when comparing simulations A7 and B7 (with a coexpanding softening of 250 kpc) to simulations A3 and B3 (with constant 250-kpc softening). Besides this effect, criterion (A4) for the integration timestep is mostly satisfied, except for the 'hard particle' (small ϵ) simulations, notably simulations B0 and B4. We just suffer from the use of hard potentials, which is most severe for B4 because ϵ was even smaller than 2 kpc (the present-epoch value) for most of the evolution. Because of the low degree of clustering, simulation A0 performs still well enough, even with a timestep that is too large according to criterion (A4). But the general conclusion for all of our simulations A0, A4, B0, B4 and C0 that employ particles which are too hard according to the maximal scattering criterion is that most of them indeed suffer from strong two-body interactions that disturb the collisionless nature of the dark matter distribution.

With respect to *coexpanding* softening we can conclude that it only works reasonably well within a rather narrow range of ϵ . For set B this is around 10a kpc (with quite a

306 E. van Kampen

Table 2. (a) Global numerical results of the Plummer softening simulations. The unit of time 'Age' corresponds to the age of the universe.

sin no		Δt_0 [Age]	$\Delta E/\Delta U$ [%]	v [km/s]	r _{nn} [kpc]	min Δt [Age]	σ_v [km/s]
A() 2	0.005	0.4	254	85	2×10 ⁻⁴	548
A1	10	0.005	0.02	254	86	8×10^{-4}	541
A2	2 50	0.02	-0.02	233	93	0.007	508
A3	3 250	0.02	-0.5	164	156	0.018	322
A	1 2 a	0.005	2.5	239	125	2×10^{-4}	520
A.	5 10 a	0.005	0.3	258	85	7×10^{-4}	556
Αć	50 a	0.02	1.2	230	106	0.009	497
A	7 250 a	0.02	3.0	190	142	0.014	411
A8	3 100	0.02	-0.1	227	95	0.008	507
D.0		0.005	2.6	(10		c: 10=5	000
BO	_	0.005	2.6	618	65	6×10^{-5}	828
B1		0.005	0.2	632	61	3×10 ⁻⁴	845
B2		0.005	0.1	587	64	0.002	792
B3		0.02	-0.4	416	83	0.004	616
B 4		0.005	8	596	75	6×10^{-5}	800
B5	10 a	0.005	1.2	621	62	3×10^{-4}	833
Be		0.005	5	584	68	0.002	787
B7	7 250 a	0.005	13	461	104	0.004	641
B8	100	0.005	-0.1	559	68	0.002	761
C) 4	0.005	0.3	832	192	9×10^{-5}	1502
C	20	0.02	0.1	810	194	5×10^{-4}	1475
C	100	0.02	0.03	758	223	0.005	1402
C:	3 500	0.02	0.5	394	322	0.015	833
C4	1 200	0.02	0.1	715	234	0.006	1363
C:	5 230 a	0.02	1.5	699	259		1284
C		0.02	0.6	803	172		1462
	**	-	- 70		- · -		

Table 2. (b) Global numerical results of the Hernquist softening simulations. The unit of time 'Age' corresponds to the age of the universe.

sim.	ϵ'		$\Delta E/\Delta U$	v	$r_{ m nn}$	$\min \Delta t$	σ_v
no.	[kpc]	[Age]	[%]	[km/s]	[kpc]	[Age]	[km/s]
A10	5.4	0.01	0.4	248	101	4×10 ⁻⁴	539
A11	27	0.01	1.8	192	120	0.003	389
A12	54	0.01	3.6	179	140	0.006	371
A13	134	0.01	8.0	179	204	0.014	223
B10	5.4	0.005	0.4	605	82	2×10 ⁻⁴	818
B11	27	0.005	1.0	551	82	9×10^{-4}	765
B12	54	0.01	3.0	423	91	0.002	655
B13	135	0.01	7.0	261	112	0.008	487
B14	27 a	0.005	6.0	542	76	9×10^{-4}	741
B15	54 a	0.005	10	523	102	0.002	723
C11	11	0.02	0.4	749	227	3×10 ⁻⁴	1436

small timestep), which is about 1/40 of the Poissonian nearest neighbour distance, or a sixth of the final nearest neighbour distance. For most constant values of ϵ the energy conservation is fine, and the timestep guessed on the basis of criterion (A4) is often even chosen to be too small (except for B0 which suffers from strong two-body encounters). Of course the criterion is a global one, and will most probably not be satisfied for all individual particles, especially the ones in very dense groups. But we can conclude that constant softening (in real space) is to be preferred over coexpanding softening. Also noteworthy in the table is the *decreasing* rms peculiar velocity v and the

total velocity dispersion σ_v within the Abell radius of the group/cluster as a function of the amount of softening, i.e. more extended particles move slower on average. This is seen in sets A and B, but most prominently in set C. We will need to take this into account when studying velocity bias (Section 5.5).

A direct consequence of this is that large-scale structure simulations that often need to use relatively large softening will find artificially reduced velocity dispersions for clusters. For example, Frenk et al. (1990) consider the cumulative distribution of velocity dispersions of a large set of clusters found in a single cosmological simulation performed using a P3M code. Because of the large volume of their box, their coexpanding softening of the P3M force law (shown in Efstathiou et al. 1985) had to be set to 560a kpc. This corresponds to $\epsilon = 230a$ kpc for a Plummer law. Simulation C5 was run with this choice of softening. Its σ_v and v are at least 15 per cent smaller than those of the less softened simulations C0, C1 and C6 (see Table 2). Because the effect is systematic, cluster velocity dispersions obtained from simulations like those of Frenk et al. can be corrected using these comparisons between runs with different amounts of softening.

For a more detailed analysis we examine the various Fourier modes at the present epoch for each simulation set. The calculated power spectra are shown in Fig. 5 for set B and in Fig. 6 for set C. The subset of ϵ chosen for Fig. 5 is $\{2, 10, 50, 250, 10a, 50a, 250a\}$ kpc. The upper curves of Fig. 5 show the power spectra as calculated in a cube with a size of half the diameter of the simulation sphere, as shown in Fig. 1(a). The lower curves 'zoom in' on the overdense structures by taking the cube to be 4 times smaller, with its precise position shown in Fig. 1(b). Fig. 6 is obtained in a similar fashion.

What is obvious from the power spectra is that there is no difference on scales larger than 1 Mpc, where the global potential well of the cluster determines the evolution, and no difference on scales smaller than 100 kpc, where the discreteness of the density distribution dominates the power spectrum. So the main differences are on the scales of subclustering, but differences between 10- and 50-kpc softening are small. The power on these scales is larger if the particles are harder, which is most obvious when we zoom in on the overdense system. Subclustering is absent for very soft particles. These results show up less prominently in simulation set A. The nearest neighbour distances, listed in Table 2(a), show the same trend but reduced to one number, giving a function $r_{\rm nn}(\epsilon)$. The main differences between sets B and C are that the differences in amplitude for the Fourier modes that do differ substantially are larger and occur at somewhat larger scales (smaller k). The clustering changes most with softening in the range 0.3 to 3 Mpc. This is probably just because all ϵ for set C are twice those of set B.

3.1.4 Hernquist softening

The Hernquist softened potential (B5) is harder than the Plummer potential (B3): when relating the corresponding scale parameter ϵ' and ϵ using (B17) or (B18) it is about twice as deep in the centre. To take half the basic timestep of the Plummer runs should roughly give a comparable precision. We reran a few of the simulations from sets A, B and C with Hernquist softening, choosing ϵ' according to equation (B17). The simulation data and resulting numbers are listed in Table 2(b).

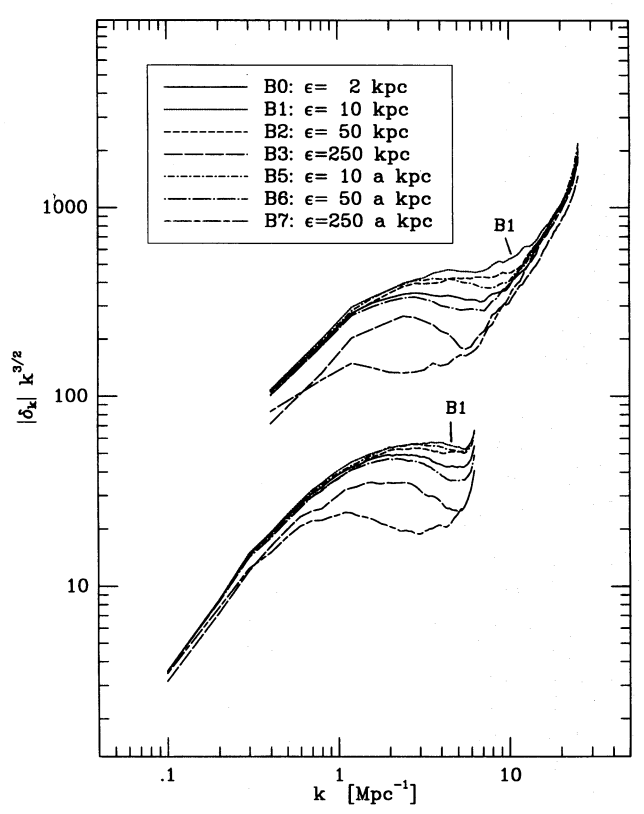


Figure 5. Final power spectra for the small cluster simulation set B. The bottom curves are measured in a central cube with a size half the radius of the simulation sphere, as indicated by the dashed square in Fig. 1(a). The top curves are obtained from a 4 times smaller cube around the small overdensity within the dashed square in Fig. 1(b), and have therefore a larger amplitude but show roughly the same effects.

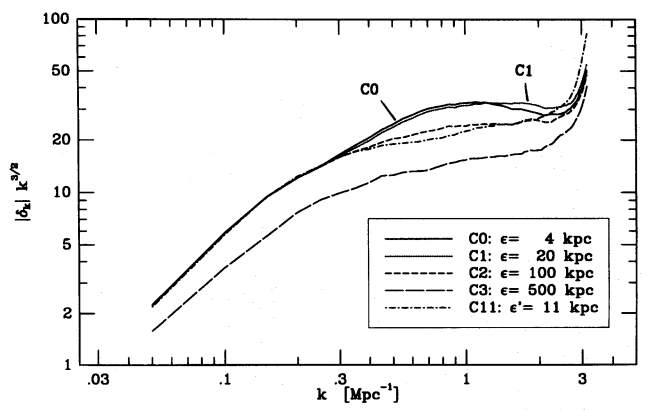


Figure 6. Final power spectra for the broad cluster simulation set C, which are measured in a central cube with an edge length half the diameter of the simulation sphere. A range of Plummer softening values and one Hernquist softening value ($\epsilon'=11$ kpc) are shown.

The first thing to notice is the increasingly poor energy conservation for increasing ϵ' . Looking at the total energy as a function of time we see that most of the energy gains/losses are during the early evolutionary phases. This must be caused by the stronger overlapping of the soft particle density profiles as compared to the Plummer particles, since the Hernquist

profile falls off less steeply than the latter. Furthermore, the energy non-conservation caused by use of coexpanding softening is even worse for Hernquist softening (see simulations B14 and B15).

As for the Plummer runs, power spectra were calculated to examine the amount of clustering on various scales. Fig. 7 shows the power spectra for set B, again taken from the box indicated in Fig. 1(a). For comparison the corresponding Plummer softening curves are plotted as well. A general difference from the Plummer runs is that the large-scale modes for the Hernquist runs deviate at a much smaller value for decreasing ϵ' than the Plummer models, for which only $\epsilon=250$ kpc shows significant deviations on large scales. For the broad cluster set C the Hernquist simulation C11 is shown amongst its counterpart Plummer runs in Fig. 6. It is seen that it follows the curve of C2, which has a Plummer softening length of 100 kpc, instead of the one it is expected to follow (because of equation (B18)): simulation C1 with $\epsilon=20$ kpc.

3.2 The softening of galaxy particles

3.2.1 Observed galaxies and dark haloes

Because we can regard soft galaxy particles as particles with a density profile, we can compare them to real galaxies by comparing their surface density profiles. One possibility is that cluster galaxies have mostly been stripped of their haloes. If so we can *directly* fit observed surface brightness profiles of ellipticals to the Plummer and Hernquist surface density model profiles (B9) and (B12) if we assume a constant mass-to-light ratio $\Upsilon \equiv \mu(R)/I(R)$, where μ is the surface density of the mass and I the surface brightness. In Appendix C we compare profiles of observed galaxies to the Plummer and Hernquist profiles. Also, profiles of interacting galaxies and dark haloes are discussed there. We summarize the conclusions here.

If we want to model average ellipticals using Plummer or Hernquist profiles we should take ϵ to be of the order of 10–25 kpc for Plummer softening and 6–8 kpc for Hernquist softening if we assume that the luminous part makes up the whole galaxy or that the dark matter distribution is equivalent to the luminous matter distribution. The Hernquist model fits best for observed single galaxies, whereas the Plummer model might provide the best fit for interacting galaxies. Most of the dark matter is probably dissipationless and its distribution therefore more extended, so we should use larger softening parameters. Since observations of dark matter haloes suffer from many uncertainties, we now look at what has been found for models of dissipationless galaxies and dark haloes.

3.2.2 Galaxy and dark halo models

What can we predict from theory for the density profiles of cluster galaxies? Since the relation between the dark and the luminous matter still is a major question of astrophysics, and dark haloes are dominating during interactions, we turn our attention to the expected shapes and sizes of dark haloes. Dubinski & Carlberg (1991) found isolated dark haloes to be quite flattened in the CDM cosmogony, with average values of 2:1.4:1 for the axial ratios. This makes them just a little more flattened than expected from Gaussian random field theory (i.e. Bardeen et al. 1986), while they are also in contradiction with shapes of luminous ellipticals deduced from observations (Franx, Illingworth & de Zeeuw 1991). For the density profile

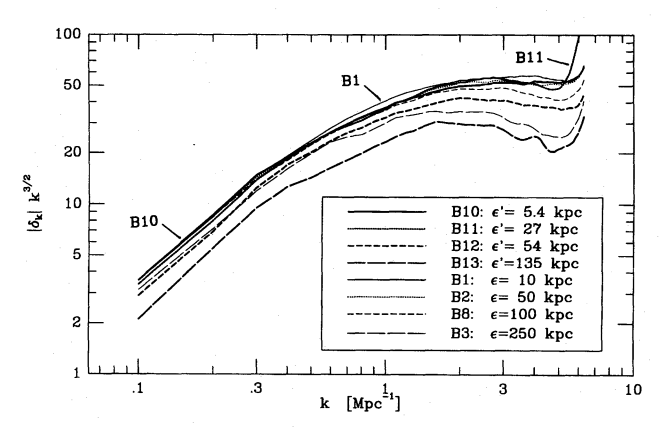


Figure 7. A comparison of Plummer and Hernquist softening for the clustering on various Fourier modes. Shown are final power spectra for selected simulations from set B, measured in the region indicated by dashed lines in Fig. 1(a).

Dubinski & Carlberg (1991) found a very good fit to the triaxial generalization of the Hernquist profile:

$$\rho(r) = \frac{M_{\rm t}\epsilon_{\rm t}}{2\pi(b/a)(c/a)} \frac{1}{r(r+\epsilon_{\rm t})^3} , \qquad (23)$$

with an average value of 27 ± 1 kpc for the geometric mean $r_t = \epsilon_t (bc/a^2)^{1/3}$ for their set of 14 simulations. Their profiles do not show a core at all, which is typical for Hernquist profiles. The mean mass M_t was found to be $10^{12.33\pm0.23}$ M_{\odot} , which is the average luminous mass of a giant elliptical. However, this might as well be the total mass of a normal elliptical including a surrounding massive dark halo. For our spherical soft particles we should then use $\epsilon' = 27$ kpc for Hernquist softening, or $\epsilon = 50$ kpc for Plummer softening when applying (B17). Note that we do not use the triaxial profile in the code, just the spherical one.

Other studies examine haloes which form in multitude in large-scale simulations (Frenk et al. 1988; Gelb 1992; SuSu; Warren et al. 1992). Only SuSu show half-mass radii of the haloes they find. Their values have a far larger dispersion than the numbers from the 14 haloes modelled by Dubinski & Carlberg (1991), which could be due to their isolated nature, enabling them to reach an equilibrium configuration. The haloes of SuSu are situated in a large-scale environment which can significantly distort them. The range of half-mass radii found by SuSu is $R_h \approx 6-50$ kpc for the same cosmological scenario as chosen for this paper (unbiased CDM, $\Omega_0=1,\ h_0=\frac{1}{2}$). One of their major conclusions is that halo properties depend heavily on the parameters of the grouping algorithm.

Many theoretical studies have been undertaken to model interacting galaxies (Barnes & Hernquist 1992 and references therein), but no consensus on the results exists. Some studies suggest that cores of galaxies are puffed up, producing a flatter central surface brightness profile. Tidal forces present in high-density environments like clusters of galaxies will tend to do this as well. It is also argued that the *outer* regions are loosened up, resulting in roughly an r^{-4} profile (e.g. McGlynn 1990). In short, this suggests a Hernquist model for large r but a Plummer model for the core. So the choice between

computationally convenient softening types for our purpose of modelling galaxies by single soft particles is not clear from this perspective.

Besides numerical models, simple analytical estimates might be used to examine the influence of typical physical processes in clusters. Physical mechanisms to inflate galaxies are grazing encounters and non-destructive tidal fields. Both puff up the galaxies by increasing their velocity dispersion, resulting in a larger galaxy of the same mass. However, tidal forces will most often strip some of the mass that was driven outwards, and might therefore change the mass more than the size. Secondary infall of mass (i.e. after the collapse which formed the galaxy) is certainly an ongoing process in clusters, increasing the size and/or mass of galaxies. However, this process is supposed to be intrinsically modelled in an N-body simulation, and should not be treated separately. The only mechanisms that reduce the size and/or mass of galaxies are evaporation, ram-pressure stripping, and tidal fields. Unfortunately we cannot model shrinking (i.e. evaporating) galaxies because of the severe numerical problems with particles that both harden and become more clustered, needing extremely short integration timesteps.

Because of the vast complexity of the physics of all these effects, both mass and size changes are neglected in this paper. In other words, we assume that all possible effects leading one way or the other more or less cancel out each other. So galaxies form from an early collapse with no subsequent events, and retain their size during the subsequent evolution of the cluster by settling to an (quasi-)equilibrium state. Very important here is that galaxy formation is likely to be a dissipational process, making such galaxies quite strongly bound entities. The dark matter in and around galaxies does not dissipate, and is less tightly bound, so galaxies could be stripped of part of their dark haloes when traversing the cluster. The choice for the sizes and masses of the galaxy should therefore mainly be guided by the luminous matter distribution, taking into account what is probably left of the halo. To take a constant physical size for our soft galaxies automatically conserves total physical energy as measured by the particles in the simulation.

The simulations by Dubinski & Carlsberg (1991) and SuSu would suggest values for ϵ that are 2 to 3 times as large as derived from the luminous part of a galaxy. Larger ellipticals, found in the cores of clusters (like M87 in Virgo), will clearly need larger values than normal galaxies. Finally we have to realize that the numerical limits on softening discussed earlier for the background particles obviously apply also to the galaxy particles.

3.3 Galaxy formation parameters p and s

The galaxy formation recipe still contains two ad hoc parameters, the basic percolation length p and the Gaussian smoothing length s, both dimensionless (see equations (6) and (7)). For lack of a good physical theory of the galaxy formation, we try several choices for the two parameters and determine which combination will do the best job. We consider the values $\frac{1}{2}$ and 1 for each parameter, yielding four combinations: $(p,s) \in \{(\frac{1}{2},\frac{1}{2}),(\frac{1}{2},1),(1,\frac{1}{2}),(1,1)\}$.

We have to bear in mind that the use of softened particles implies that the standard virial theorem does not apply. Because the pair interaction potential is softened, the total potential energy of the systems will be smaller, and the same is true for the kinetic energy. We should use the Clausius Virial instead, which for Plummer potentials reads

$$\sum_{i} m_{i} x_{i} \cdot \ddot{x}_{i} = 2T + U + \frac{1}{2} \sum_{i,j} \frac{G m_{i} m_{j} \epsilon^{2}}{(|x_{j} - x_{i}|^{2} + \epsilon^{2})^{3/2}} , \qquad (24)$$

where the rightmost term just represents the energy stored in the soft particles, $T = \frac{1}{2} \sum_{i} m_{i} v_{i}^{2}$ is the total kinetic energy and $U = \frac{1}{2} \sum_{i} m_{i} \phi_{i}^{Pl}$ is the total potential energy of the particle distribution, with the Plummer potential ϕ_i^{Pl} given by (B3). This implies that the larger the softening, the larger 2T+U becomes because the rightmost term of (24) varies roughly as $1/\epsilon$. Interestingly, most of the energy gained is put into potential energy. In fact, an increase of ϵ results in even more extra potential energy than the amount gained, because the kinetic energy decreases. These changes are illustrated in Fig. 8, which shows the total, kinetic and potential energies for the final distributions of the simulations as a function of the (non-expanding) softening parameter adopted. Most of the kinetic energy change must be in groups, where the softening length matters most. Groups normally satisfy (9), but this effect means a shift of $M(2.5R_h\sigma^2/G)$ to smaller M. On the other hand, softening will increase the half-mass radii of groups since soft particles cluster less tightly. The latter effect causes a slight shift to larger masses. Therefore the combined effect is hard to predict, and we will examine it for several of the simulation sets.

For set B, we plot in Fig. 9 the mass M of the resulting groups as a function of $2.5R_h\sigma^2/G$ at z=2 for four choices of ϵ with $p=\frac{1}{2}$ and s=1. Only groups with at least 10 particles are shown, since groups with less members are too noisy (compare to Fig. 4). Criterion (9) is shown as a straight line. Before drawing any conclusions on the effect of softening as discussed, we have to realize that not all of the groups identified by the grouping algorithm will be in virial equilibrium in the first place. Apparently the second – enlarging – effect seems to dominate for small ϵ . However, the first clearly dominates for large ϵ by significantly decreasing the group velocity dispersion σ . This is confirmed by the global root-mean-square peculiar velocities listed in Table 2. The \sqrt{N} -noise on the quantities is evident in the figure, where low-mass groups consisting of only a few particles scatter heavily around the supposed relation, but the high-mass groups do well. We conclude that most of the more massive groups are in virial equilibrium or at least bound $(4GM > 5R_h\sigma^2)$, with a few still collapsing (indicated by a large velocity dispersion).

We next examine what the choices for p and s imply for the groups found by the local density percolation technique. Fig. 10 shows the particles of simulation B1 ($\epsilon = 10$ kpc) that reside in groups containing at least 10 particles at z = 2 for the set of (p, s) defined above, and where these particle end up. This gives us an idea which particles residing in early-formed groups survive the formation of structures like clusters of galaxies, and how this depends on the choice for (p,s). A small value for p will pick out only the cores of groups, and the chance of survival will increase. Fig. 10 confirms this for groups outside the main cluster for $p = s = \frac{1}{2}$. A larger p will include less bound particles around the core as well, yielding more realistic groups because criterion (9) is more easily satisfied, mainly resulting from a better coverage of local phase space. By including more loosely bound particles the chance of survival for the whole group decreases, as can be seen in Fig. 11 for the two p = 1 cases. As noted earlier (compare to Fig. 3),

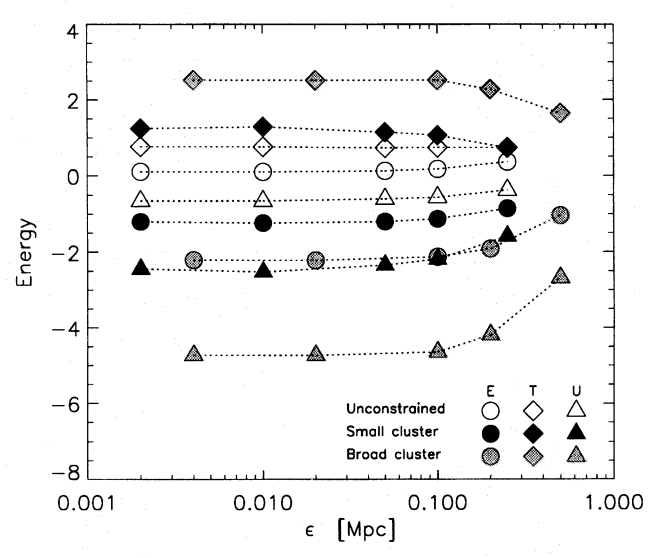


Figure 8. System binding (E), kinetic (T) and potential (U) energies (with arbitrary units) as a function of the softening parameter ϵ for the final distributions of the simulations from set A (open symbols), B (filled symbols) and C (grey symbols) with *constant* ϵ .

groups ending up in the cluster are completely disrupted, and for these the choice of (p, s) does not matter.

The disruption of galaxies should be even more devastating within clusters. We examined test set C, the broad cluster model, to investigate this. In the spirit of the previous discussion we plotted scatter diagrams of $2.5R_{\rm h}\sigma^2/G$ against M at z=2 for simulation C1 together with its Hernquist softening counterpart C11 (the two are related by equation (B17)). As for set B, we found that at z=2 most groups identified by the local density percolation technique are indeed physical groups. The scatter plots (not shown) indicate that there is no significant difference, except that there might be somewhat more scatter for the Hernquist softening run.

3.4 Upper and lower mass cut-offs

When making galaxies we need to restrict masses to a probable mass interval. The lower cut-off is determined by the noise clearly visible at the low-mass end of scatter plots of $2.5R_h\sigma^2/G$ against M. Only Fig. 4 shows this noisy part as well; we omitted it in Fig. 9. One should choose the lower cut-off at the mass level where the points are not scattered too much out of the factor-of-two region around the virial line. For the upper cut-off we should try to find a physical transition scale, for example the scale above which dissipation is not important and galaxies are not easily formed. However, since not much is known on the exact physics of galaxy formation, a number for such a scale length is difficult to obtain, so we will try to use observations instead. We could use the bright end of the average (or joint) cluster luminosity function to estimate the expected brightness of the brightest galaxy, and link this to its mass, giving the desired upper mass cut-off. Unfortunately, there are many uncertainties involved which can change this value by an order of magnitude, such as the Hubble parameter h_0 , the cosmological density parameter Ω_0 , the mass-to-light ratio and the colour of the galaxies.

Instead we use the observed mass of M87, the brightest cluster elliptical (BCE) of the Virgo cluster, as the maximum

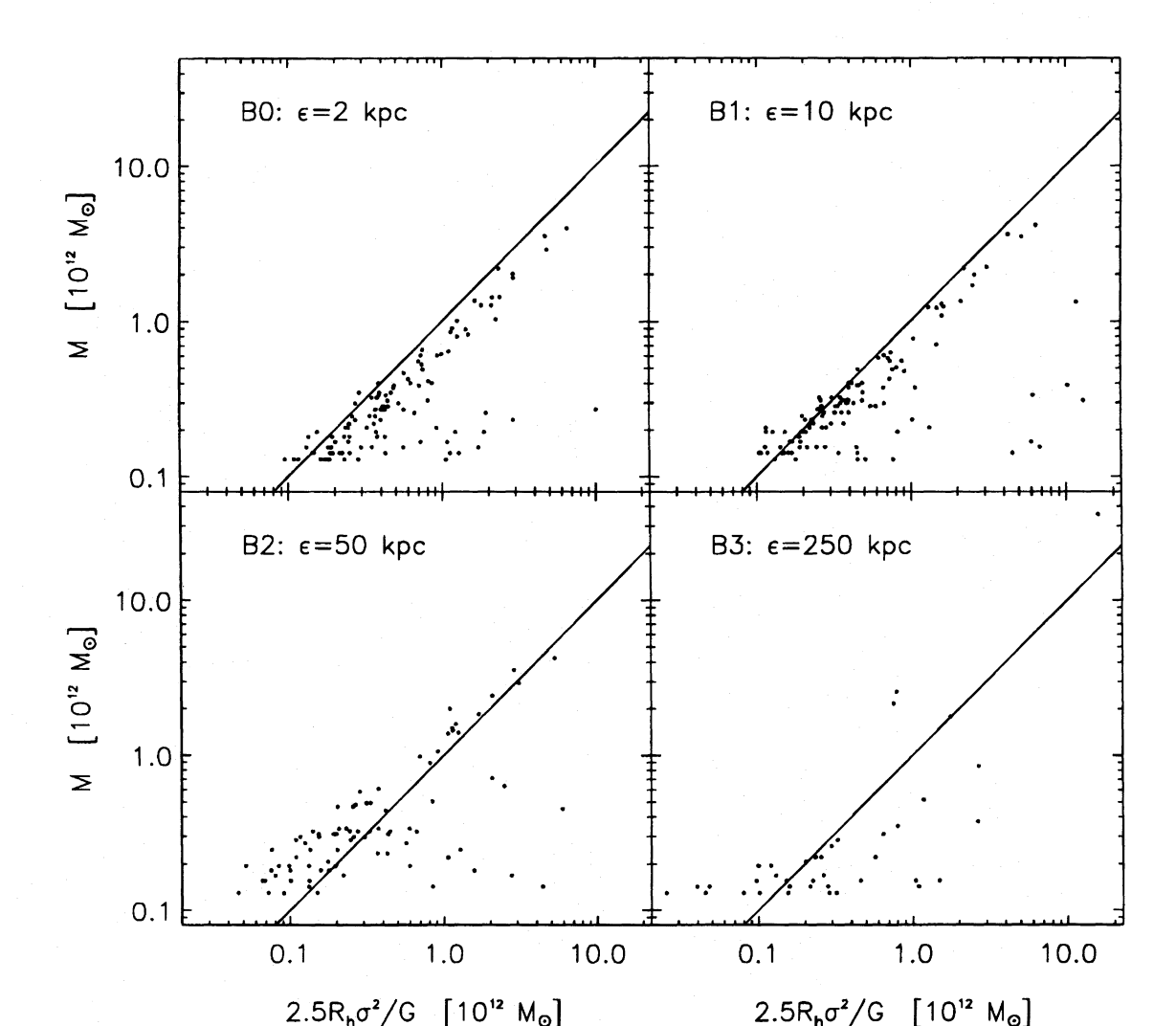


Figure 9. The mass M of groups of more than 10 particles as found by the local density percolation technique with s=1 and $p=\frac{1}{2}$ against $2.5R_h\sigma^2/G$ for four choices of ϵ , plotted for the small cluster simulations of set B at z=2.

allowable single particle mass. This is a few times $10^{13}~M_{\odot}$, with a factor of two uncertainty (see Appendix C). For other clusters a mass estimate for their BCE does not exist. However, if the number of original particles is still quite large for somewhat smaller galaxy masses, we decide on the basis of the applicable disruption time whether to replace such a group by a single particle or model it by the original equal-mass particles. We expect that in general this situation will only occur for $N_{\rm ig} > 10\,000$, which is not the case for most of our present models. We therefore do set the upper mass cut-off to a few times $10^{13}~M_{\odot}$, with the precise value depending on the specific simulation set and galaxy formation epoch, as will be discussed for each individual model.

4 GALAXY FORMATION AND CLUSTER EVOLUTION

4.1 Instant galaxy formation at z=2

We can now test our proposed solution for the numerical disruption problem with galaxies in clusters, in which we form galaxies during the cluster evolution by replacing groups by a single particle at a certain epoch. We adopt a simplification here, as a first step, by making galaxies 'instantly' at a certain redshift. This approximation will only break down if the process is not peaked at all in redshift space. It is really unknown when the bulk of the galaxies formed (e.g. Rees 1991), but as a first test we make galaxies instantly at z=2. This value is in between the era where most of the quasars are found (e.g. Schmidt, Schneider & Gunn 1986), and the present epoch, where galaxies could still be forming. Recent work by Cen & Ostriker (1992) encourages our choice: they found that – at least within the CDM scenario – galaxy formation might be peaked around z=2-3.

We use the small cluster simulation B1 from the previous section, the broad cluster simulation C1, the (similar) simulation pair D1 and D2, and the very rich cluster simulation E1. All simulations are run through to the end as traditionally done, but are also paused to form galaxies, and resumed with the newly formed galaxies and the remaining background particles together. In simulation B1 we need 60 particles in a group to constitute the mass of a typical galaxy

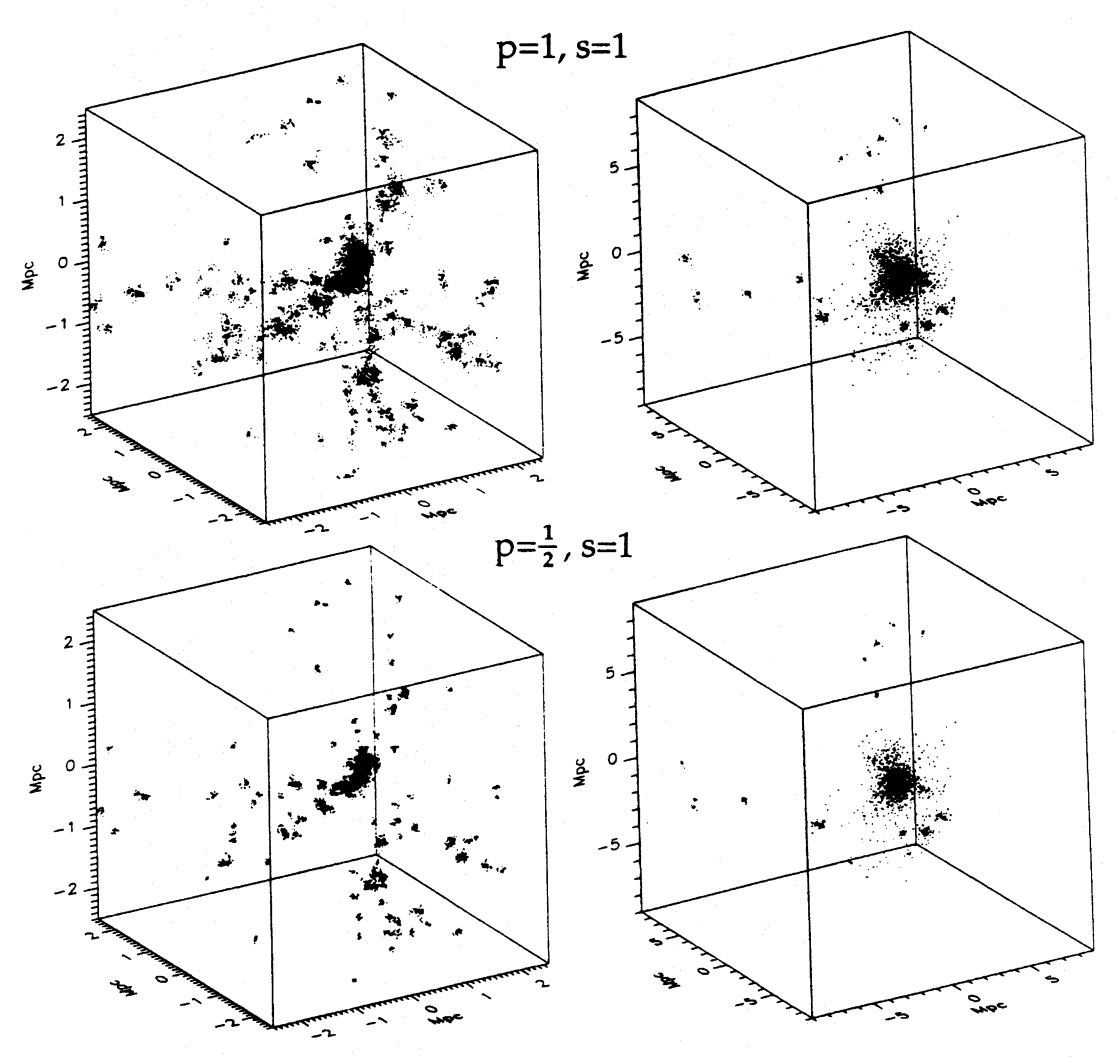


Figure 10. 3D-plots of particles in groups with more than 10 particles, for different choices of the local density percolation parameters for the small cluster simulation B1. The left hand cubes show their positions at z = 2; the right hand cubes show their present positions.

like our own (with the assumption of a dark halo out to 100 kpc, Hills 1985). Only 7 particles are needed to make up the galactic mass for C1. Set D has both of these resolutions for similar initial conditions, to test resolution effects. All parameters as well as some results are listed in Table 3.

We discuss the small cluster simulation B1 first. In fact we consider three simulations: B1, which is just the plain run with equal-mass particles, and B1a and B1b, which have galaxies formed at z = 2 as described, with $(p,s)=(\frac{1}{2},1)$ for B1a and (p,s)=(1,1) for B1b. Both choices, and in fact almost any choice, result in one massive galaxy at the centre of the proto-cluster, which just collapsed at z = 2, as shown in Fig. 11(a). This should correspond to the early formation of a massive cD galaxy. For the first choice of p the massive galaxy is retained, with a mass of $4{\times}10^{13}~M_{\odot},$ which just exceeds our imposed upper mass limit, but is still possible. For the second choice of p the particles remain loose, although the would-be galaxy almost satisfies (9), being marginally bound. We make this distinction between B1a and B1b in order to examine the difference this makes. When forming the remaining galaxies, only groups with a mass larger than 2.4×10^{11} M_{\odot}, i.e. consisting of at least 14 unit-mass particles, are selected. This choice is based on the scatter in Fig. 9. The mass spectra of the galaxies found are plotted in Fig. 16 (Section 5) for both B1a and B1b, showing that the larger percolation parameter p results in more massive galaxies.

The galaxies themselves are shown in Fig. 11(b) for B1a and Fig. 11(c) for B1b. The size of the circles that represent the individual galaxies is proportional to $M^{1/3}$. The loose dots shown are particles which were tagged to reside in groups by our local density percolation technique, but did not fulfill the virial criterion (9). We clearly see that this criterion indeed removes odd groups for which local density percolation still suffers from the defects of the ordinary percolation technique. Figs 11(d) and 11(e) show the resulting initial conditions for simulations B1a and B1b respectively, which are just the formed galaxies plus the remaining simulation particles sampling the dark matter. Evolution of these to the present epoch results in the final matter distributions shown in Figs 12(a) and 12(b), which are to be compared to Fig. 1. It is apparent that simulations B1a and B1b with galaxies formed at z = 2 have a less concentrated mass distribution than the cluster with no early galaxy formation. We will quantify this later in Section 5.

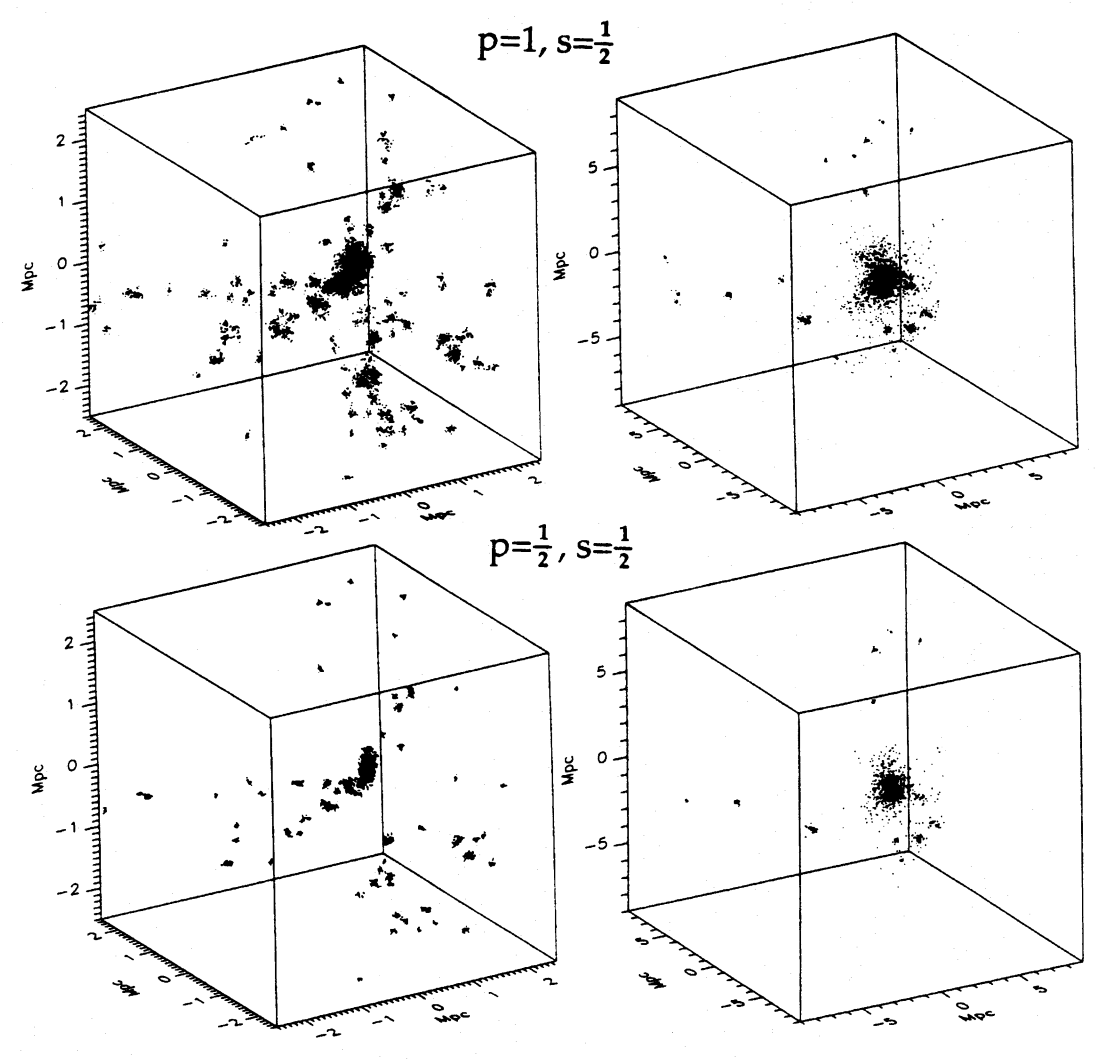


Figure 10 - continued

When identifying galaxies at the present epoch, we might argue that the percolation parameters chosen at z = 2 should be used again at the present epoch. It has to be remarked. however, that the physical state of the system could differ significantly, so that different percolation parameters might be required. Because of the higher degree of clustering, the average nearest neighbour distance is smaller and identical percolation parameters will tag more particles as group members. Furthermore, identified groups at the present epoch will on average be more massive than groups identified at higher redshifts. Despite using the local density in the linking method, the smooth nature of the dark matter distribution at late times in the simulation, caused partly by numerical effects and tidal stripping, will either cause all particles to be linked up as one large group, or result in no extra groups at all. There is of course often a large cD galaxy observed in a cluster, but it is questionable if identification of such a cD galaxy in a model calculation should be done by the local density percolation method, considering that cD haloes are huge and smoothly connect to the surrounding group or cluster (Porter, Schneider & Hoessel 1991; Kemp & Meaburn 1991). The largest problem is that many of the traversing galaxies, as identified at z=2, are scooped up as well, while they should remain

separate entities because of their large velocities (dispersions up to 1500 km s⁻¹ have been measured), ensuring their survival.

We apply local density percolation with the same values as at z = 2 plus the virial criterion (9), resulting in the cluster models shown in Figs 12(c) and 12(d). Trying these very same grouping parameters on the final distribution of the original plain simulation B1 (see Fig. 1), we end up with the models displayed in Figs 12(e) and 12(f). The criterion again removes a few odd groups as at z = 2, so the method itself seems to work well at the present epoch also. However, Fig. 12 clearly shows the impossibility of identifying new (i.e. recently formed) galaxies within the cluster at the ends of all three simulations, because all small-scale structure is destroyed by numerical effects. For B1 we noticed violent relaxation of the collapsing cluster, which results in a smooth density distribution with a dense core. Simulations B1a and B1b do not show such a dense core, but the dark matter distribution is smooth as well. When inspecting the evolution of this distribution we see no violent relaxation in these early galaxy formation models, suggesting that galaxy formation might suppress violent relaxation.

Table 3. Parameters and results of the galaxy formation simulations.

sim. no.	^Z form	number of particles	р	s	m _{min} [10 ¹²	m _{max} ² M _☉]	$f_{ m gal}$	$\frac{M_{ m est}/M_{ m real}}{(R_{ m Abell})}$	$M_{ m est}/M_{ m real} \ (R_{ m turn})$	$\sigma_{ m gal}$ [km s ⁻¹]	σ _{dark} [km s ⁻¹]	R _{hm,gal} [Mpc]	R _{hm,dark} [Mpc]
B1	-	19042	-	-	-	_	-	-	<u> </u>		845	_	0.91
B1a	2	12937	$\frac{1}{2}$	1	0.24	40	0.32	0.78	0.71	527	721	1.39	2.00
B1b	2	13131	1	1	0.24	11	0.23	0.60	0.58	628	756	1.06	1.46
C1	· -	18125	-	-	·		_	_	· · · · · · -	-	1474	- .	1.87
C1a	4	15194	$\frac{1}{2}$	1	0.95	20	0.17	0.49	0.42	1195	1449	0.93	2.60
C1b	2	14399	$\frac{\tilde{1}}{2}$	1	0.95	25	0.21	0.66	0.54	1379	1481	0.95	2.56
C1c	1	13932	$\frac{\overline{1}}{2}$	1	0.95	35	0.24	2.77	2.28	1609	1367	2.88	2.28
C1d	4/2/1	11803 [†]	$\frac{1}{2}$	1	0.95	72	0.36	1.06	0.90	1291	1375	2.00	3.49
C11	_	18125	_	_	_	٠	_	_	· · · · · · · · · · · · · · · · · · ·	_	1450		
C11a	2	13234	$\frac{1}{2}$	1	0.95	35	0.27	0.74	0.63	1503	1433		
D1		146654	_	_	_	_	<u>-</u>	· · · · · · · · · · · · · · · · · · ·		_	1319		2.75
D1a	4	126769	1	1	0.51	10	0.14	0.56	0.44	1281	1307	1.63	3.44
D1b	2	119007	1 2	1	0.51	13	0.19	0.96	0.79	1559	1446	2.33	2.58
D2	-	18405	- -	-	-		-	-	0.75	-	1394	2.33	2.55
D2a	4	15893	$\frac{1}{2}$	1	0.95	19	0.14	0.52	0.33	1234	1340	1.10	3.45
D2b	2	14708	$\frac{1}{2}$	1	0.95	13	0.20	0.53	0.40	1086	1305	1.75	3.92
E1	_	139743	_	_		_	_	· . <u>-</u>		_	2912	_	5.67
E1a	4	127040	$\frac{1}{2}$	1	0.95	19	0.12	0.93	0.57	2556	2832	4.22	6.51
E1b	2	111004	1 2	1	0.95	41	0.24	1.75	0.98	3127	2833	6.60	5.68
E1c	4/2/1	102380 [†]	$\frac{1}{2}$	1	0.95	41	0.30	1.30	0.80	2870	2813	6.30	5.93

[†] number of particles after last galaxy formation step

4.2 The epoch of galaxy formation

When forming galaxies 'instantly' at one specific redshift, there might very well be a dependence of the resulting models on the formation redshift. We investigate this for the test simulation C1. The fast collapse of the main overdensity observed for set B will not occur for simulation C1, because the cluster was constrained to be broad, implying a longer time-scale for the collapse. In fact it turns out that it just collapses in two roughly equal clumps at the end of the run, the first originating from the centre where the 2σ constraint was put, and the other from the outer regions of the simulation sphere. Such large-scale merging is inevitable in hierarchical clustering scenarios like CDM, but for our testing purposes the amount of merging is reduced artificially for C1 by taking 'broad' constraints (as described in 2.1).

Here we test only one choice for the percolation parameters: $(p,s)=(\frac{1}{2},1)$, also used for simulation B1a. The main motivation for these values is that we only want to replace the central part of the halo by a single particle. The outer parts are thus kept loose to allow for possible tidal stripping. We find that most of the groups satisfy virial criterion (9), and have half-mass radii in the range 15–80 kpc, i.e. Plummer softening parameters in the range 12–60 kpc. This is the expected range for dark halo sizes, i.e. 2–3 times the extent of the luminous component (Appendix C).

Galaxies are formed at four different redshifts: z=4, z=2, z=1 and z=0 (the present epoch). The last choice is included to compare with traditional N-body modelling in which galaxies are identified in the final distribution. Snapshots from the standard run C1 at these redshifts are shown from left to right in the top row of Fig. 13. The galaxies found at

the corresponding epochs are displayed in the middle row of the same figure. These distributions, except that of the present epoch, are then used as initial conditions for simulations C1a, C1b and C1c. For simulation C1b the most massive group is not replaced by a single particle because its mass would be $6\times10^{13}~M_{\odot}$, while for simulation C1c the two most massive groups are not replaced either for the same reason. It should be noted that the introduction of two very massive particles is not handled very well by the N-body integrator: in a test run the two massive particles evolved into a close binary system causing strong evaporation of the rest of the particles by slingshots!

The end results are shown in the bottom row of Fig. 13. Identification of galaxies at the present epoch is again found to be impossible. Experimenting with the percolation parameters, we found that to take the same parameters as at z = 2 causes a large fraction of the matter to end up in a single large group. To take half the values for both p and s produces almost no extra groups and merges hardly any existing groups. We again observe that these kinds of galaxy identification methods do not work at z = 0 within large-scale overdensities like clusters, because both the dark matter and the galaxy distribution are very smooth due to the numerical effects discussed before. However, since velocities are large $(\sigma_v > 1000 \text{ km s}^{-1})$ and the intra-cluster medium is hot, we can also argue that both galaxy formation and merging of single galaxies (not of subgroups of galaxies!) more or less ceased within clusters. We can then assume that the distribution found at the end of the runs can be considered to be the final result. We will make this assumption and use these distributions for further analysis, i.e. refrain from identifying galaxies at the final epoch.

314

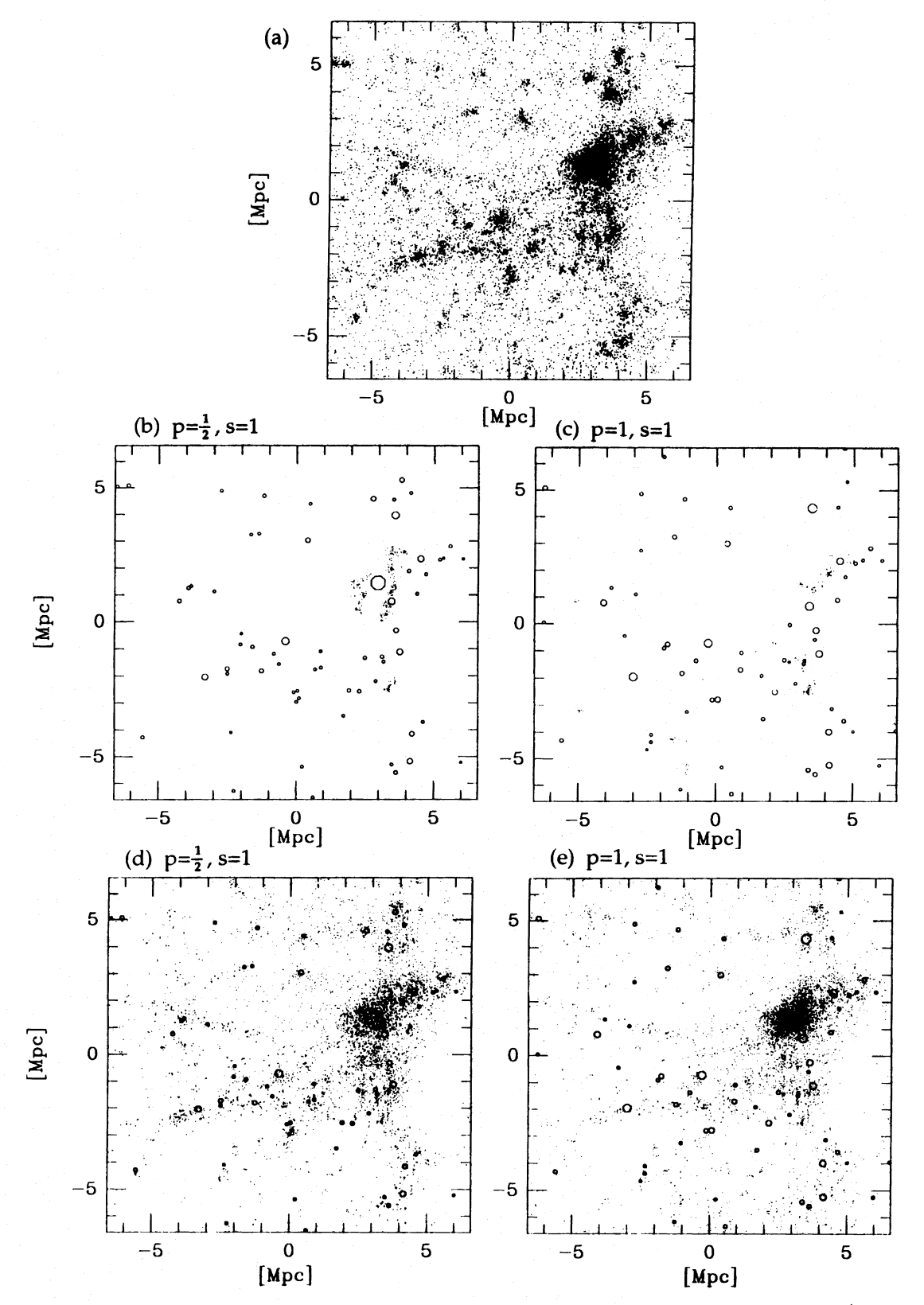


Figure 11. (a) Distribution of the small cluster simulation B1 at z=2. (b) Groups (indicated by circles) found for $p=\frac{1}{2}$, s=1. The dots indicate particles that were tagged as a group by the percolation algorithm, but whose groups were too far from virial equilibrium to be real. (c) As (b), but for p=s=1. (d) As (b), but with the remaining loose particles that make up the background dark matter distribution. (e) As (d), but for p=s=1. The latter two distributions are used as initial conditions for simulations B1a and B1b respectively.

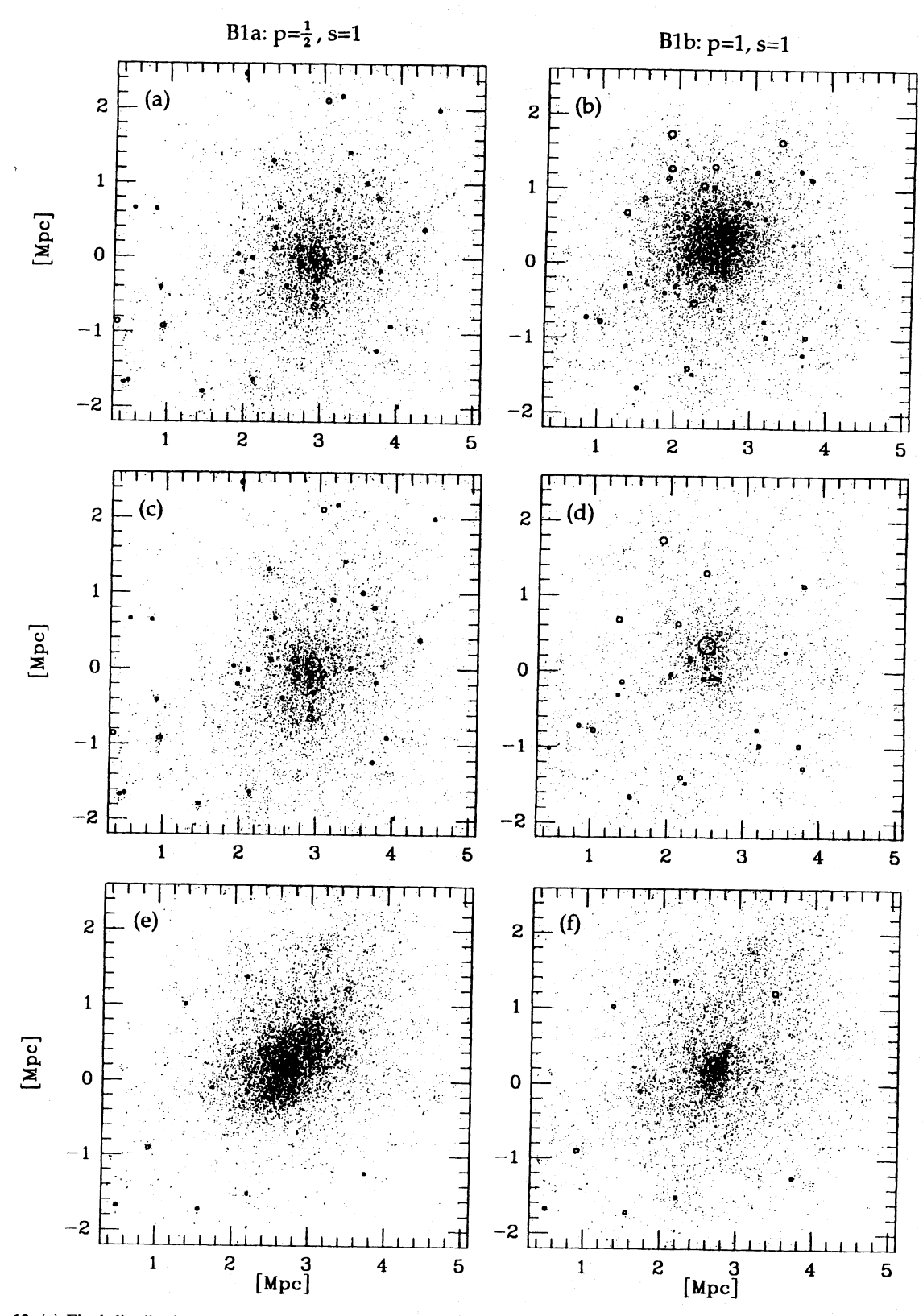


Figure 12. (a) Final distribution of the small cluster simulation B1a. (b) As (a), but for for simulation B1b. (c) Galaxies identified in B1a at the present epoch for $(p,s)=(\frac{1}{2},1)$, after applying virial condition (9) within a factor of two (see text for details). (d) As (c), but for B1b with (p,s)=(1,1). (e) As (c), but for the plain run B1 with $(p,s)=(\frac{1}{2},1)$. (f) As (e), but for (p,s)=(1,1).

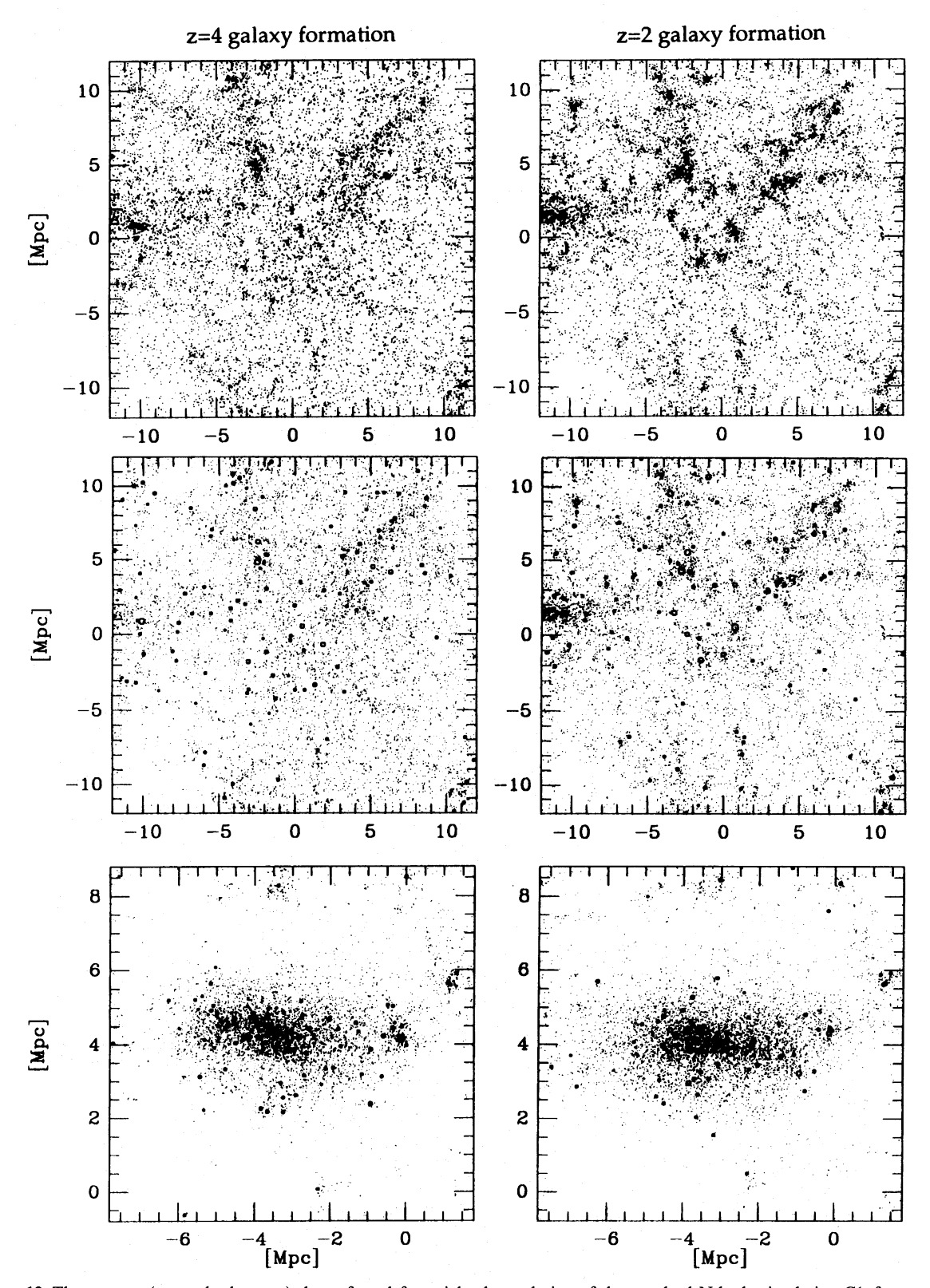


Figure 13. The top row (across both pages) shows from left to right the evolution of the standard N-body simulation C1, for z = 4, z = 2, z = 1 and z = 0. The middle row shows the resulting galaxies and remaining dark matter when using local density percolation plus virial condition (9) within a factor of two at these redshifts. The bottom row (note the different frame size!) shows the end results of the distributions shown in the middle row.

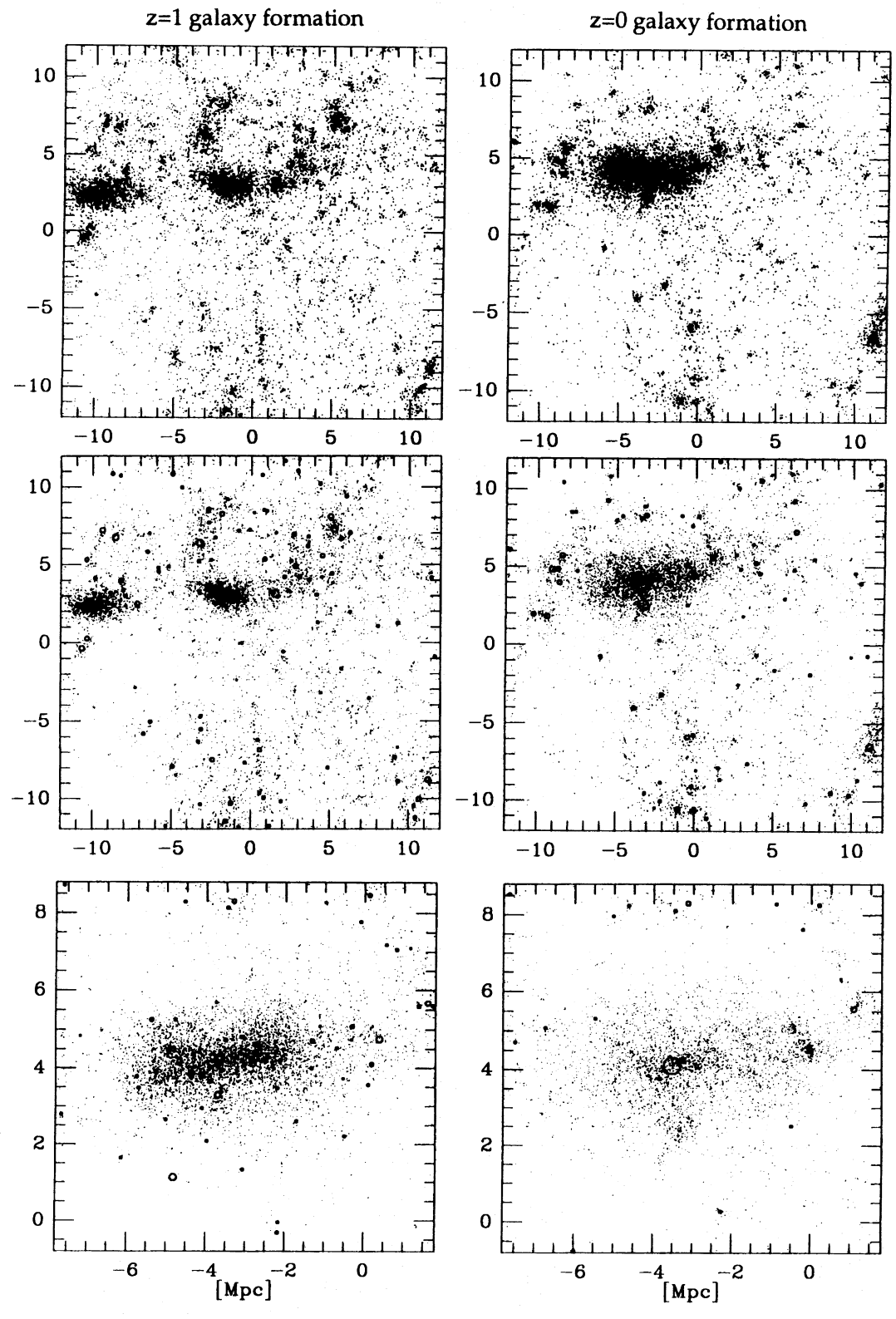


Figure 13 - continued

A first look at these final distributions reveals immediately that the concentrations of the resulting galaxy distributions are very different for different formation epochs. The dark matter distribution is roughly similar for the different runs,

but its most important feature is the lack of a dense core, as was observed for set B as well. Also note that for the late-formation model (z=1) there are relatively many massive galaxies outside the main cluster, whereas for early galaxy

318 E. van Kampen

formation most massive ones are to be found in the central parts of the cluster.

4.3 Resolution issues again

We found in Section 2.3 that an increase of the number of particles does not help very much to preserve groups of simulation particles within overdensities like clusters of galaxies. But are our proposed solutions hampered by resolution effects? High- and low-resolution set D is used to try to understand this, i.e. we ask whether simulation sets D1 and D2 produce statistically the same results. Fig. 14 shows the two resulting galaxy distributions, with and without the dark matter distribution. One gets the impression of a slightly more compact distribution of galaxies for the low-resolution simulation D2 (quantified in Section 5.2). We observe an alignment of both the low- and high-resolution distributions. Furthermore, when one smooths the distribution with a Gaussian filter of a few Mpc the overdensities are very similar with respect to shape, amplitude and size. The low-resolution simulation lacks the group of galaxies which is present in the high-resolution counterpart at (x, y) = (-3.8, -2.5) Mpc in the bottom left panel of Fig. 14. However, most of that mass is still visible in the top right panel of Fig. 14 as dark matter plus a somewhat more massive galaxy. This example illustrates that the detailed distribution of mass amongst galaxies and dark matter is different for different resolutions, but that the global distribution is very similar. Statistical properties should therefore be similar as well.

4.4 Continuous galaxy formation and evolution

A logical next step is to make the galaxy formation process more continuous while still using the relatively simple methods presented above. This can be done by repeating the galaxy formation step at several redshifts, creating new galaxies and allowing the ones formed earlier to gain mass by grouping them together with surrounding dark matter particles or other galaxies. The latter option means that we can include merging, which is certainly an important process during the early evolutionary stages of a cluster. Simulations C1a and E1a are used for this purpose. The grouping algorithm is applied at $z = \{4, 2, 0.8, 0.25\}$, resulting in simulations C1d and E1c. The final distribution of the latter is shown in Fig. 15. Again, very massive groups are not replaced by single soft particles. An upper mass limit of 3×10^{13} M_{\odot} is maintained here. When comparing these models with the ones for galaxy formation at one specific redshift, we see them to behave as an intermediate case. Clearly, grouping of particles with different masses is more complicated than for equal-mass particles. Around a massive particle the smoothed density field has a large amplitude, causing the percolation length to be quite small and making it difficult to link it to other particles. It is also more softened, loosening its gravitational grip on its surroundings.

5 PROPERTIES OF THE RESULTING CLUSTERS

We will present some global results for the model groups and clusters built, although they need not be representative for a typical cluster. However, the inclusion of galaxy formation and preservation enables us to study various effects of cluster evolution that deserve a closer look.

5.1 Calculating cluster properties

Extraction of cluster properties from model calculations is clearly much easier than from observations, since for models the full phase-space information is available and the mass spectrum is known. Although a wealth of information is contained in cluster simulations, some quantities remain ambiguous to define, like the centre of the cluster, or its mass. We chose the cluster centre to be the position of the maximum in the density field smoothed with a Top-Hat filter of 3 Mpc, which is the Abell radius (Abell 1958). After obtaining the cluster centre, we can calculate spherically averaged profiles like the mass density profile and the velocity dispersion profile. In this paper we restrict ourselves to inspection of global parameters and overall behaviour of the resulting clusters, and indicate where the models should be further improved. We will discuss cluster luminosity functions and total masses in some detail, and also investigate various biases and mass segregation.

5.2 Global properties

5.2.1 Luminosity functions

In Fig. 16 we plot the mass functions n(M) that resulted directly from the formation of galaxies in our models from the sets B, C, D and E. We see that these mass functions have a power-law shape, with an indication of an exponential cut-off at the high-mass end for set E. Recall that we applied an upper mass cut-off in our galaxy formation recipe, so the observed mass cut-off is inherent to the models. However, no shape information was used.

For a constant mass-to-light ratio we can compare the shapes of our mass functions to observed luminosity functions. Various forms for the luminosity function n(L) have been fitted to observed clusters. The Schechter (1976) function is a good fit for field galaxies as well as for cluster galaxies (Colless 1989) and has a reasonable physical explanation in a cosmological context (Press & Schechter 1974; Bond et al. 1991). Another form is that proposed by Abell (1975), consisting of two power laws mimicking a break at a certain scale. It only fits well for clusters of galaxies, which have relatively more bright galaxies than the field (Rhee 1989).

The Abell function does not fit too well for our models: the slope is somewhat too shallow, mostly due to the deficiency of low-mass galaxies. A Schechter function with characteristic mass $M^*\approx 9\times 10^{12}~\rm M_\odot$ and $\alpha=-1.25$ fits the mass functions of set E quite well, as shown in Fig. 16. Because set B is a group, and sets C and D are not typical clusters, these three sets are not expected to compare well to average observed clusters. The transition from mass M^* to absolute magnitude $M_{B_T}^*$ obviously depends on Ω_0 , h_0 and the mass-to-light ratio Υ . In our $\Omega_0=1$ and $h_0=\frac{1}{2}$ models the M^* found for set E corresponds to the observed $M_{B_T}^*\approx -21.5$ (Felten 1985) for a constant mass-to-light ratio of $300\Upsilon_\odot$. Because our galaxy particles include dark haloes, this is a reasonable number (the brightest Virgo elliptical M87 has probably $\Upsilon=750\Upsilon_\odot$, see Appendix C).

5.2.2 Density and velocity dispersion profiles

In this section we look at the density and velocity dispersion profiles of the model clusters, both for the galaxies

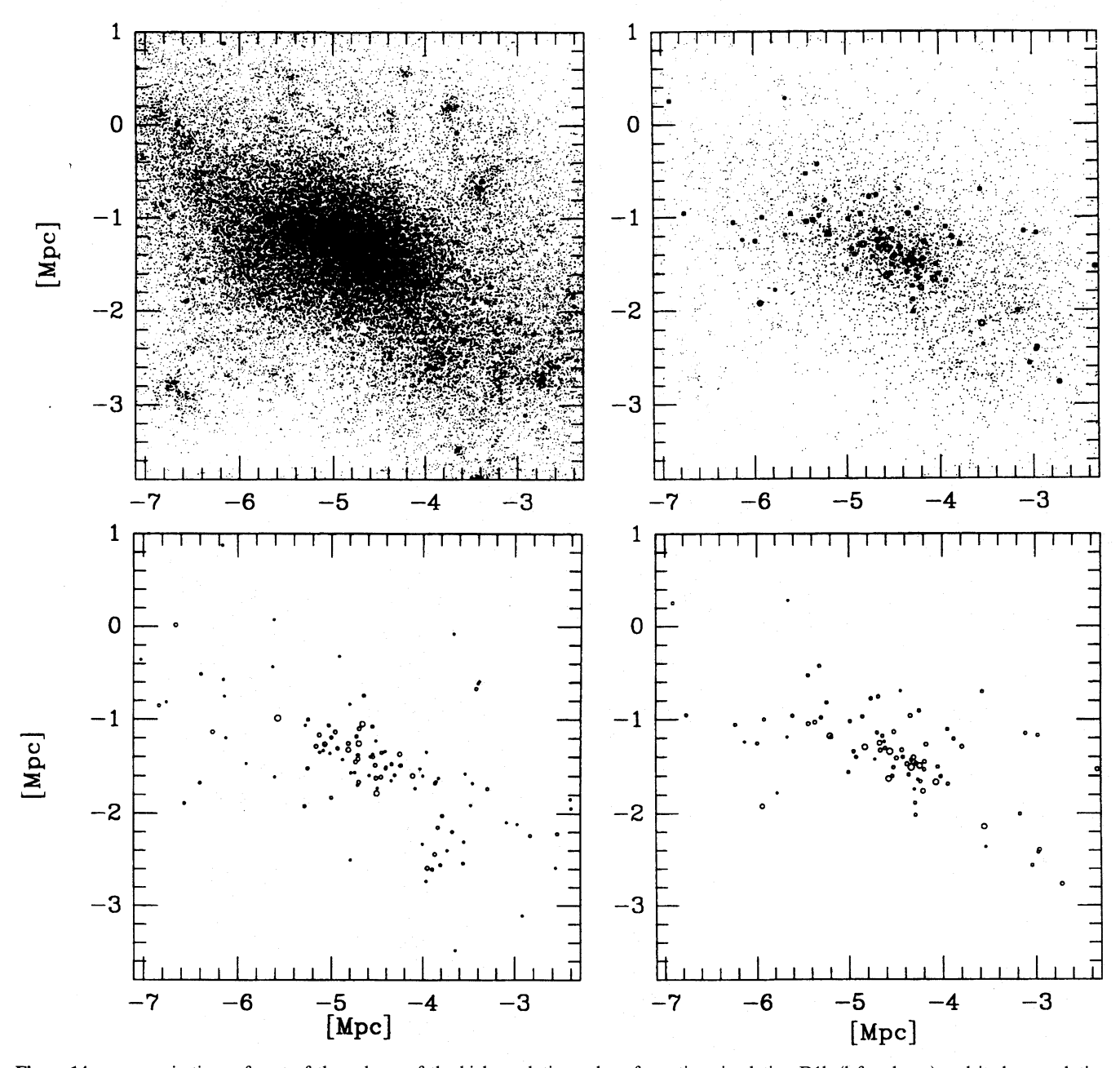


Figure 14. x - y projections of part of the volume of the high-resolution galaxy formation simulation D1b (left column) and its low-resolution counterpart D2b (right column) at z=0. The top row shows galaxies plus dark matter, the bottom row only the galaxies.

and for the dark matter. They are plotted in Fig. 17 for sets D1, D2 and E. The density profiles for the galaxies, represented by dotted lines, and for the dark matter component, shown as solid lines, are renormalized according to their mass fraction. The runs without galaxy formation are shown as dashed lines. For the density profiles we see a clear separation of the galaxy and dark matter components with respect to the original run without galaxy formation, where the galaxies cluster most (note that the plots are logarithmic!). The differences in the velocity dispersion profiles of the two components are less clear; it appears that the galaxy component is slightly colder. The velocity dispersions are rather large, especially for set E. This is a known

problem of the unbiased CDM scenario (e.g. Frenk et al. 1990).

5.2.3 Total mass

A truly global property of a cluster is its total mass. However, it is difficult to define, just like a cluster itself. As in Table 1, where the global properties of the standard simulation sets are listed, we will use the Abell radius as well as the more physical turnaround radius. It is interesting to see to what extent these masses can be reproduced by the various mass estimators as used for observed (projected) data, where only the luminous component is known. We limit ourselves to a comparison of

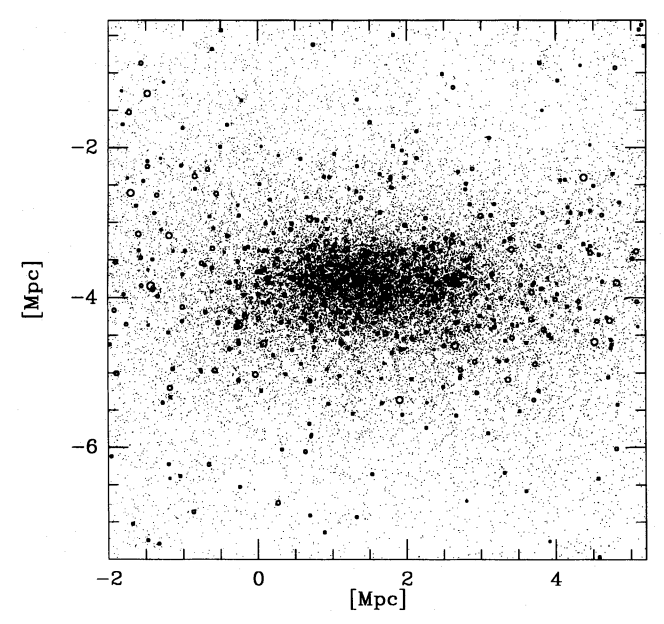


Figure 15. Final distribution of the 'continuous' galaxy formation simulation E1c, a very rich cluster.

the total mass, obtained from the 6D phase-space distribution of galaxies, to the real mass. The virial mass estimator

$$M_{\rm vir} = \frac{2R_{\rm hm}\sigma_v^2}{G} \tag{25}$$

(e.g. Saslaw 1985) uses the mass-weighted mean harmonic radius

$$R_{\rm hm} = \frac{\left(\sum_{i} m_{i}\right)^{2}}{2\sum_{i} \sum_{j < i} \frac{m_{i} m_{j}}{r_{ij}}} \tag{26}$$

and the total velocity dispersion (also weighted with mass)

$$\sigma_v^2 = \frac{\sum_i m_i v_i^2}{\sum_i m_i} \ . \tag{27}$$

Table 3 lists the ratio of estimated mass to real mass obtained within both the Abell radius and the turnaround radius for all our galaxy formation cluster models. We see that masses are mostly underestimated for *early* galaxy formation, and overestimated for late galaxy formation (notably simulation C1c). We consider this result in more detail below.

The results of set D show that the high- and low-resolution simulations give roughly the same ratios for z=4 galaxy formation, but disagree for z=2 galaxy formation. This indicates that resolution effects become increasingly more important when the amount of clustering increases. We might solve this by applying the more continuous galaxy formation approach, as discussed in Section 4.4.

5.3 Mass segregation

Because we form galaxies within a sea of dark matter early on, we can search for mass segregation effects, i.e. a difference in concentration between the dark and luminous matter during the subsequent evolution. West & Richstone (1988) found that

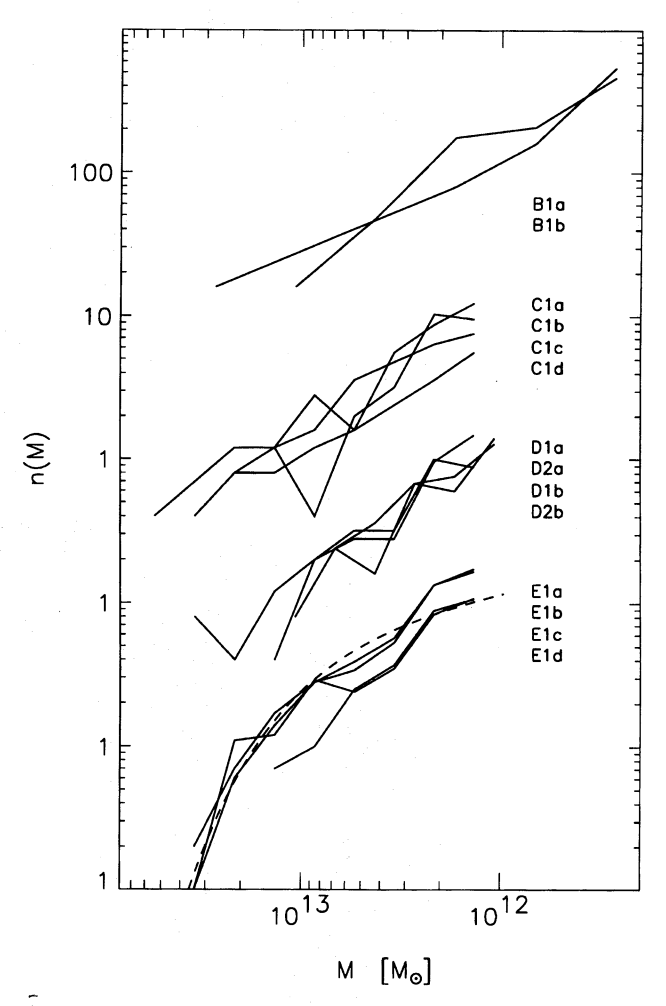


Figure 16. Mass functions for the simulation sets B, C, D and E, renormalized for the simulation volumes, and multiplied by decreasing factors of 10 for each set for clarity. The dashed line is a Schechter function with $M^* \approx 9 \times 10^{12} \ \mathrm{M}_{\odot}$ and $\alpha = -1.25$. It fits the mass functions of set E quite well.

the luminous matter, in the form of galaxies, clusters more strongly than the dark matter, which was represented by 100 times less massive particles. This results in an error in the virial mass estimate: West & Richstone claim that this could be up to a factor of 10 too low, and that the segregation is mostly caused by dynamical friction. This was confirmed by Serna, Alimi & Scholl (1993) using higher resolution models.

It is, however, likely that the dark matter also settles in clumps with a mass large enough to reduce the differences between luminous and dark matter significantly, and therefore also reduce the effect of dynamical friction on the galaxies. The amount of mass segregation will therefore depend on the fluctuation spectrum of the dark matter. A scenario like CDM will show much less segregation than the West & Richstone (1988) and Serna et al. (1993) white noise simulations, whereas hot dark matter (HDM) could show a similar or larger effect if galaxies form early enough. Generally the mass of a galaxy particle is about ten times as large as that of a dark matter particle. However, we assume that our galaxies, once formed, do not lose mass. If mass loss is significant, our cluster galaxies might suffer too much dynamical friction. We will search for mass segregation with this uncertainty in mind.

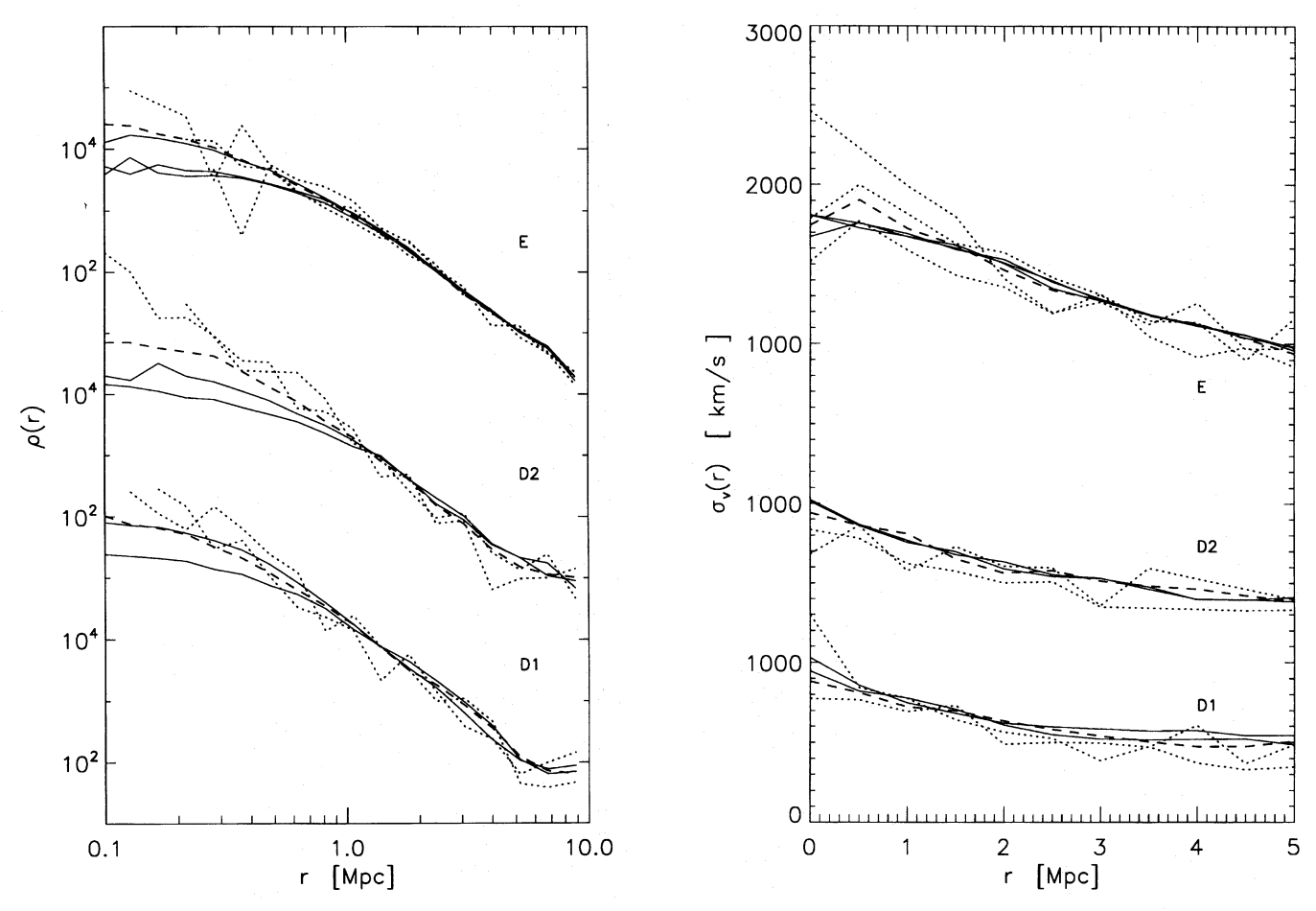


Figure 17. Density and velocity dispersion profiles of the final cluster models from the simulations sets D1, D2 and E. For reasons of clarity we use different normalizations for each set. Dotted lines represent galaxies, solid lines the dark matter distribution. Both are renormalized according to their mass fraction. Dashed lines denote simulations without galaxy formation.

A simple measure of mass segregation is the mean harmonic radius (26) of the cluster, which has both the disadvantage and advantage of being a single quantity. It depends on the radius within which it is calculated, but can easily be plotted as a function of time. In Fig. 18(a) we utilize this to see mass segregation at work for simulations D1a and D2a. We compare mean harmonic radii for the galaxies (thick lines) and the dark matter (thin lines) within the cluster turnaround radius (as obtained for the present epoch: see Table 1) in the comoving frame. Table 3 lists the present-day harmonic mean radii for the two mass components for all models run.

We find no significant initial segregation for C1a and C1b, but there is a rather large *inverse* initial segregation for C1c. The latter effect is dominated by the choice *not* to replace the largest two concentrations of particles by a single soft particle (see Section 4.2). Therefore $R_{\rm hm}$ for the dark particles is dominated by these remaining concentrations and is considerably smaller than that for the galaxies. The formation of galaxies in the C1c model at z=1 is troublesome anyway because two-body disruption has done much damage already to groups that should still exist at that time. For C1a and C1b, the mean harmonic radii separate considerably during the evolution after the formation epoch, and the final segregation amounts to a factor of 2.5 at the present epoch. For C1c the rather large inverse segregation quickly diminishes, but does

not disappear. An increase of the resolution reduces the final segregation somewhat, as demonstrated by the plots for set D, but not by a large amount.

For the very rich cluster set E, galaxy formation at z = 2(model E1b) results in the same initial inverse segregation effect we observed for z = 1 galaxy formation for the much poorer broad cluster (model C1c). For both these models one might argue that this formation epoch is just too late, i.e. many galaxies got disrupted before our instant formation epoch. We do believe that the segregation effect is real and significant for the models with galaxy formation before or at z = 2. It causes a general underestimation of the total mass (see Table 3 for the corresponding numbers), but the effect we observe is certainly not as strong as that found by West & Richstone (1988) and Serna et al. (1993). So indeed our CDM models show less segregation than their white noise simulations. But we cannot resolve the issue of mass loss with the present modelling, so the amount of segregation found should be considered as an upper limit.

5.4 Biases in and around clusters

5.4.1 Cluster spatial bias

The observed mass segregation might be of interest on a cosmological scale, since it produces a bias between galaxies

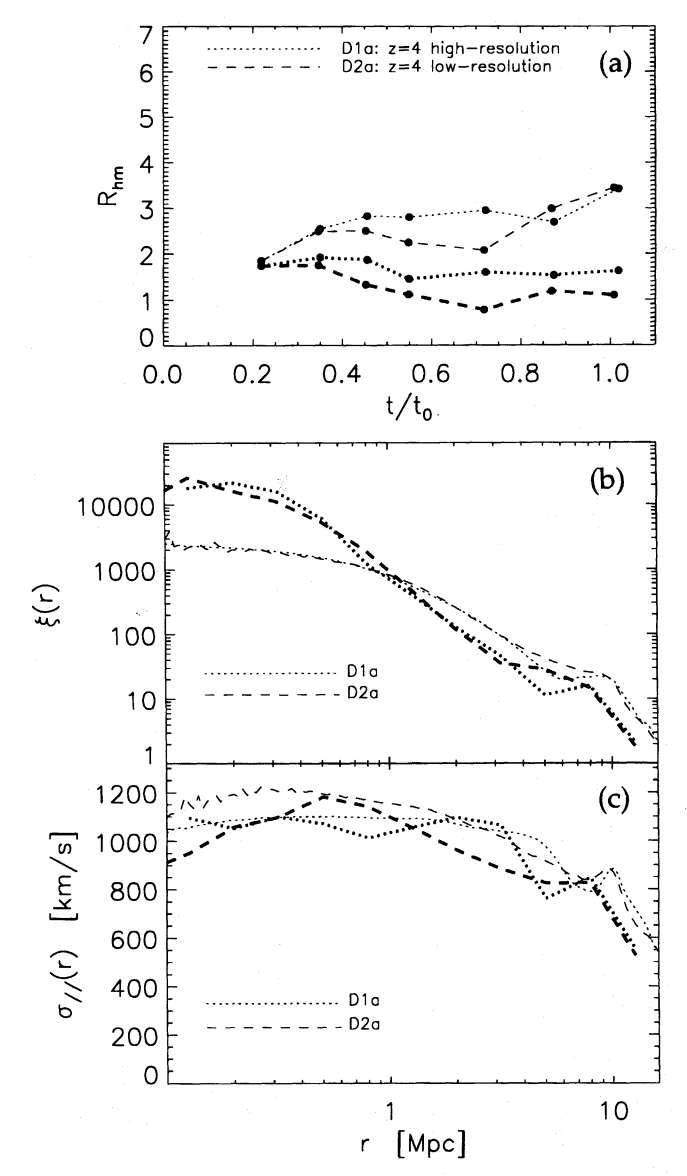


Figure 18. (a) Mass segregation for the z=4 galaxy formation simulations from set D, expressed by the mass-weighted mean harmonic radii within the turnaround radius for both the galaxies (thick lines) and the dark matter (thin lines). (b) Comparison of the two-point correlation functions for galaxies (thick lines) and dark matter (thin lines) within the turnaround radius around the cluster centre for the z=4 galaxy formation simulations from D. (c) Pairwise velocity dispersions, plotted similarly to (b).

and the underlying mass distribution. We have to discriminate between the different types of spatial bias defined in the literature. There is the original idea of peak bias, which is of purely statistical origin and stems from thresholding the density fluctuation field (Kaiser 1984). If this field is Gaussian distributed, as we assume it to be in the early universe, clustering of peaks above a certain threshold v times the rms fluctuation σ_0 is stronger than that of the field itself, as quantified by their representative two-point correlation functions:

$$\xi_{\rm gal}(r) \approx \frac{v^2}{\sigma_0^2} \xi_{\rm all}(r) \ . \tag{28}$$

This is only an approximation; the full expression is more complicated. We will not discuss the full machinery here, but refer to Peacock (1992) for an excellent review. To take (28) as the exact description is called *linear* bias, fully described by one quantity b, i.e. $\xi_{\rm gal}(r) \equiv b^2 \xi_{\rm all}(r)$. In fact, this means that

$$\frac{\delta n}{n} = b \frac{\delta \rho}{\rho} \,\,, \tag{29}$$

where n represents the number density of galaxies and ρ the compound mass density. Finally there is the so-called *natural* bias, as proposed by White et al. (1987), which is the difference in clustering between dark matter and haloes selected on the basis of their maximum circular velocity. We will not examine this any further in the present discussion, but just search for a possible linear bias by examining the difference between the correlation functions found for the dark matter particles and for the galaxies. Both were calculated using the method described in Section 3.1.2.

We search for a possible bias within the turnaround radius of our cluster models, a region that contributes much to the small-scale part of the cosmological two-point correlation function. Fig. 18(b) shows the correlation functions for both galaxies and dark matter within this radius for the models D1a and D2a, two similar models with galaxy formation at z = 4at different resolutions. A clear bias is observed, largest for early galaxy formation, which is shown in the figure. Within 1 Mpc the bias amounts to a factor of 2 to 3, rendering it an important effect for the virial mass estimator since it will dominate the mean harmonic radius. There is a slight anti-bias for the late galaxy formation models (C1c and E1b, not shown), which explains the overestimation of their total mass using the virial estimator. Our simulations show a bias that is not linear; the slope of the correlation function is different for both mass components. By simulating clusters we have a biased sample of the universe, but it has been argued that the cosmological autocorrelation function is dominated by the contribution from regions of radius 10 Mpc centred on the cluster (McGill 1991). Still, we might suffer from other systematics, like the fact that we form galaxies instantly at a relatively early epoch. If we allow galaxies to form at late times as well, then they preferentially form outside clusters, thus enhancing our measured galaxy autocorrelation function at large r. So we need better modelling to reach a more definite conclusion.

5.4.2 Cluster velocity bias

An important recent issue is the possible existence of velocity bias (Carlberg, Couchman & Thomas 1990; Bertschinger & Gelb 1991; Gelb 1992), especially within clusters of galaxies (Carlberg 1994). If it occurs, it could solve the problem that the standard CDM model has in generating too large small-scale pairwise velocity dispersions (seen in standard N-body models), which are dominated by the contribution from cluster members. Velocity bias can be expressed in several forms. One definition is the ratio of the dispersion profile of the galaxies to that of the dark matter. More frequently used is the ratio of their pairwise velocity dispersions $\sigma_{\parallel}(r)$. The pairwise velocity dispersion is defined as

$$\sigma_{\parallel}(x) \equiv \langle (v_{\parallel} - \langle v_{\parallel} \rangle)^2 \rangle^{1/2} \tag{30}$$

(e.g. Gelb 1992), with the relative velocity

$$v_{\parallel} \equiv (\mathbf{v}_i - \mathbf{v}_i) \cdot (\mathbf{x}_i - \mathbf{x}_i) / |\mathbf{x}_i - \mathbf{x}_i| . \tag{31}$$

All quantities were obtained while calculating the spatial correlation function $\xi(r)$. A single-value velocity bias can be found by comparing central velocity dispersions for both mass components. They are listed in Table 3 for all models. The largest effect is found for simulations C1a and E1a, which had their galaxies formed at z=4: both the velocity dispersion and $\sigma_{\parallel}(<1, \mathrm{Mpc})$ for the galaxies are 80–90 per cent that of the dark matter.

This amount of velocity bias is quite small, however, and it cannot compensate for the rather large spatial bias in order to get the virial mass estimate (25) right. The underestimation of the total mass by the virial estimator is therefore mostly caused by the spatial clustering bias of dark and luminous matter. Because of the amount of noise, no firm statement on the presence of velocity bias in clusters of galaxies can be made, except for the z = 4 galaxy formation models. Fig. 18(c) shows that the high/low-resolution simulation pair D1a/D2a (with galaxies formed at z = 4) shows a bias as well (at both resolutions), but its significance is hard to address. A severe problem is the $v(\epsilon)$ effect encountered in Section 4: softer particles have somewhat smaller velocities. Since our galaxy particles are always softer than the dark matter particles, this might account for the entire velocity bias effect in our models!

Important in the comparison of these results to the original Carlberg et al. (1990) result is that there is a rather large statistical effect present in their estimate, as pointed out by Gelb (1992). In their calculation of the dark matter pairwise velocity dispersion they *included* particles tagged as residing in galaxies, raising the dispersion on small scales. Exclusion of these particles diminishes the velocity bias, but does not remove it completely, certainly not on the scale of clusters of galaxies. Obviously we do not suffer from this statistical effect. Because we are looking at clusters instead of an average patch of universe, we find much larger $\sigma_{||}$ than do both Carlberg et al. and Gelb. For the same reason we cannot directly compare the shapes of the curves found.

6 CONCLUSIONS

We have shown that standard N-body methods are not well suited for the study of clusters of galaxies because of the numerical two-body and physical tidal disruption of their member galaxies. This results in a smooth distribution of matter at the present epoch in which it is impossible to identify galaxies. Such is obviously not desired since observed clusters still contain very many galaxies. The disruption can be prevented by replacing groups of particles that represent galaxies by single soft particles at a certain epoch, as a simple approximation to dissipational galaxy formation. We can then continue to integrate the evolution of these soft galaxy particles along with the remaining particles, which model the dark matter distribution.

To define groups, we use a local density percolation technique, which is a much improved version of ordinary percolation. The groups found are replaced by a single particle if they satisfy the virial equilibrium criterion to within a factor of two. This freedom is necessary due to numerical noise in small groups, and because we are dealing with soft particles for which the Clausius Virial applies. Local density percolation plus this equilibrium criterion is shown to be very well suited for the purpose of identifying galaxies.

The softening parameter of a new galaxy particle is proportional to the half-mass radius of the group it replaces. This makes the choice of the softening parameter much better motivated than by just taking a value that is numerically convenient. The sizes of our galaxies are reasonable when comparing them to observations. Unfortunately we are still forced to base our choice for the softening of the (dominating) dark matter component on numerical considerations because we do not know the nature of the dark matter. We find that the actual choice influences the amount of substructure within clusters on the scale of 0.1 to 1 Mpc.

Various types of clusters have been built by making galaxies 'instantly' at a certain redshift. This assumes that the bulk of galaxy formation takes place at this redshift. An attempt to identify new galaxies in these models at the present epoch fails just as it does for standard N-body simulations, because both the dark matter and the galaxies are again distributed smoothly. The current method does not incorporate merging of galaxies. However, this can be done by applying the group finder several times during the evolution, thus making the galaxy formation process more continuous. In a first test with galaxy formation at four different redshifts it is shown that this gives results that are intermediates of the 'instant' galaxy formation models at these redshifts. The group finder we use in this paper is as yet not really suited for grouping particles with different masses and sizes, but this can easily be improved upon. Resolution tests show that low-resolution simulations give similar results to high-resolution ones if galaxies are made early enough, which is promising for the continuous galaxy formation method if we start early enough, so that we can accept a rather low resolution. This allows us to use a smaller timestep for the numerical integration, or to run many different realizations of a class of cluster models.

The mass functions for model set E, the rich clusters, are in reasonable agreement with observed luminosity functions if a constant mass-to-light ratio is assumed. The other sets do not contain 'typical' cluster models and therefore have more deviant mass functions. Virial mass estimates using only the galaxies are mostly underestimates because of mass segregation between luminous and dark matter. When we examine differences between formation epochs by making galaxies at z = 4, z = 2 and z = 1, it is found that clusters with galaxies that formed at high redshifts have their galaxies presently more clustered than clusters with galaxies formed at a later epoch. A clear spatial bias is observed within the turnaround radius for most of the formation epochs, whereas velocity bias is only significant (but still small) for z = 4 galaxy formation. The latter might even be completely artificial due to the effects of softening.

ACKNOWLEDGMENTS

I would like to thank (in alphabetical order) Ray Carlberg, Roland den Hartog, Peter Katgert, Nico Roos, Michael West, Rien van de Weygaert, Simon White, and Tim de Zeeuw for useful suggestions, comments and discussion. Joshua Barnes and Piet Hut are gratefully acknowledged for allowing use of their treecode, Edmund Bertschinger and Rien van de Weygaert for providing their constrained random field and Hoffman-Ribak codes, and EelcoSoft Software Services for partial financial support.

324 E. van Kampen

REFERENCES

Aarseth S.J., 1963, MNRAS, 126, 223

Aarseth S.J., Fall S.M., 1980, MNRAS, 236, 43

Abell G.O., 1958, ApJS, 3, 211

Abell G.O., 1975, in Sandage A., Sandage M., Kristian J., eds, Stars and Stellar Systems IX: Galaxies and the Universe. University of Chicago Press, Chicago, p. 601

Allen A.J., Richstone D.O., 1988, ApJ, 325, 583

Amram P., Sullivan W.T., III, Balkowski C., Marcelin M., Cayatte V., 1993, ApJ, 403, L59

Ashman K.N., 1992, PASP, 104, 1109

Bardeen J.M., Bond J.R., Kaiser N., Szalay A.S., 1986, ApJ, 304, 15

Barnes J.E., Hernquist L., 1992, ARA&A, 30, 705

Barnes J.E., Hut P., 1986, Nat, 324, 446

Beers T.C., Forman W., Huchra J.P., Jones C., Gebhardt K., 1991, AJ, 102, 1581

Bertschinger E., 1987, ApJ, 323, L103

Bertschinger E., Gelb J.M., 1991, Comput. Phys., 5, 164

Binggeli B., Tammann G.A., Sandage A., 1987, AJ, 94, 251

Binney J.J., Tremaine S.D., 1987, Galactic Dynamics. Princeton Univ. Press, Princeton

Bond J.R., Cole S., Efstathiou G., Kaiser N., 1991, ApJ, 379, 440

Caldwell J.A.R., Ostriker J.P., 1981, ApJ, 251, 61

Carlberg R.G., 1994, ApJ, 433, 468

Carlberg R.G., Couchman H.M.P., Thomas P.A., 1990, ApJ, 352, L29

Carney B., Latham D.W., 1987, AJ, 93, 116

Cen R., Ostriker J.P., 1992, ApJ, 399, L113

Colless M., 1989, MNRAS, 237, 799

de Zeeuw P.T., 1992, in Longo G., Capaccioli M., Busarello G., eds, Morphological and Physical Classification of Galaxies. Kluwer Academic Publishers, Dordrecht, p. 139

Dickey J.J., 1988, ed., ASP Conf. Ser. Vol. 5, Minnesota Lectures on Clusters of Galaxies and Large Scale Structure. Astron. Soc. Pac., San Francisco

Dubinski J., Carlberg R.G., 1991, ApJ, 378, 496

Efstathiou G., Davis M., Frenk C.S., White S.D.M., 1985, ApJS, 57, 241

Evrard A.E., 1990, in Oegerle W.R., Fitchett M.J., Danly L., eds, Clusters of Galaxies. Cambridge University Press, Cambridge, p. 287

Evrard A.E., Summers F.J., Davis M., 1994, ApJ, 422, 11

Fabricant D., Gorenstein P., 1983, ApJ, 267, 535

Farouki R.T., Salpeter E.E., 1982, ApJ, 253, 512

Felten J.E., 1985, Comments Astrophys. Space Sci., 11, 53

Ferguson H.C., Sandage A., 1990, AJ, 100, 1

Fitchett M.J., 1990, in Oegerle W.R., Fitchett M.J., Danly L., eds, Clusters of Galaxies. Cambridge University Press, Cambridge, p. 111

Forman W., Jones C., 1982, ARA&A, 20, 547

Franx M., Illingworth G., de Zeeuw P.T., 1991, ApJ, 383, 112

Frenk C.S., White S.D.M., Davis M., Efstathiou G., 1988, ApJ, 327, 507

Frenk C.S., White S.D.M., Efstathiou G., Davis M., 1990, ApJ, 351, 10

Gelb J.M., 1992, Large Simulations of Gravitational Clustering in the Universe. Ph.D. Thesis, MIT

Heisler J., White S.D.M., 1990, MNRAS, 243, 199

Hernquist L., 1987, ApJS, 64, 715

Hernquist L., 1990, ApJ, 356, 359

Hernquist L., Barnes J.E., 1990, ApJ, 349, 562

Hills J.G., 1985, AJ, 92, 595

Hockney R.W., Eastwood J.W., 1981, Computer Simulation Using Particles. McGraw-Hill, New York

Hoffman Y., Ribak E., 1991, ApJ, 380, L5

Huang S., Dubinski J., Carlberg R.G., 1993, ApJ, 404, 73

Kaiser N., 1984, ApJ, 284, L9

Katz N., White S.D.M., 1993, ApJ, 412, 455

Kemp S.N., Meaburn J., 1991, MNRAS, 251, 10P

Kormendy J., 1977, ApJ, 218, 333

Little B., Tremaine S., 1987, ApJ, 320, 493

McGill C., 1991, MNRAS, 250, 340

McGlynn T.A., 1984, ApJ, 281, 13

McGlynn T.A., 1990, ApJ, 348, 515

Mamon G.A., 1987, ApJ, 321, 622

Merritt D., 1988, in Dickey J.J., ed., ASP Conf. Ser. Vol. 5, Minnesota Lectures on Clusters of Galaxies and Large Scale Structure. Astron. Soc. Pac., San Francisco, p. 175

O'Dea C., Uson J.M., 1986, eds, Radio Continuum Processes in Clusters of Galaxies. NRAO, Greenbank

Peacock J.A., 1992, in Martinez V.J., Portilla M., Sáez D., eds, New Insights into the Universe, Lecture Notes in Physics Vol. 408. Springer-Verlag, Berlin, p. 1

Plummer H.C., 1911, MNRAS, 71, 460

Porter A.C., Schneider D.P., Hoessel J.G., 1991, AJ, 101, 1561

Press W.H., Schechter P., 1974, ApJ, 187, 425

Rees M.J., 1991, Phys. Scr., T36, 97

Rhee G.F.R.N., 1989, The Structure of Rich Clusters of Galaxies:Clues to Formation and Evolution. Ph.D. Thesis, RijksuniversiteitLeiden, chapter 8

Sarazin C.L., 1986, Rev. Mod. Phys., 58, 1

Saslaw W.C., 1985, Gravitational Physics of Stellar and Galactic Systems. Cambridge University Press, Cambridge

Schechter P., 1976, ApJ, 203, 297

Schmidt M., Schneider D.P., Gunn J.E., 1986, ApJ, 310, 518

Serna A., Alimi J.M., Scholl H., 1993, preprint

Smith H., Jr, 1992, ApJ, 398, 519

Spitzer L., Jr, 1969, ApJ, 158, L139

Stewart G.C., Canizares C.R., Fabian A.C., Nulsen P.E.J., 1984, ApJ, 278, 536

Suginohara T., Suto Y., 1992, ApJ, 396, 395 (SuSu)

Suto Y., Cen R.Y., Ostriker J.P., 1992, ApJ, 395, 1

Turner E.L., Aarseth S.J., Gott J.R., III, Blanchard N.T., Mathieu R.D., 1979, ApJ, 228, 684

van Albada T.S., Bahcall J.N., Begeman K., Sancisi R., 1985, ApJ, 295,

van de Weygaert R., 1991, Voids and the Geometry of Large-Scale Structure. Ph.D. Thesis, Rijksuniversiteit Leiden, chapter 2

van de Weygaert R., Bertschinger E., 1994, preprint

van de Weygaert R., van Kampen E., 1993, MNRAS, 263, 481

van Haarlem M., van de Weygaert R., 1993, ApJ, 418, 544

Warren M.S., Quinn P.J., Salmon J.K., Zurek W.H., 1992, ApJ, 396, 395

West M.J., Richstone D.O., 1988, ApJ, 335, 532

West M.J., Dekel A., Oemler A., 1989, ApJ, 336, 46

White S.D.M., 1976, MNRAS, 177, 717

White S.D.M., Davis M., Efstathiou G., Frenk C.S., 1987, Nat, 330, 451

Whitmore B.C., Forbes D.A., Rubin V.C., 1988, ApJ, 333, 542

Wright G.S., James P.A., Joseph R.D., McLean I.S., Doyon R., 1990, in Sulentic J., Keel W.C., eds, Proc. IAU Colloq. 124, Paired and Interacting Galaxies. NASA Conference Publication, p. 321

APPENDIX A: THE N-BODY SET-UP

The numerical code used is a slightly adapted version of the Barnes & Hut (1986) treecode. Because of the high densities involved in clusters, and because of their geometry (a hierarchy of clustering), this code is the appropriate choice here. Although the initial conditions are generated in a periodic cube, we chose to have a perfectly homogeneous universe around the simulation volume. This prevents possible artificial effects from having a grid of clusters, as is the case with periodic boundary conditions. It is necessary to cut a sphere out of the

initial cube with this choice, because a cube will have its corners collapse less rapidly than the points in between, causing an unphysical deformation of the simulation volume. With no boundary conditions we lack tidal forces from inhomogeneities around the simulation sphere, so the outer shell of a simulation is not to be trusted and will be neglected in the analysis. We use, physical instead of comoving coordinates (mostly used in large-scale structure simulations), because clusters of galaxies have turned around against the overall expansion of the universe. This makes the use of physical coordinates more appropriate, but also necessitates a modification for the choice of the integration timestep: it needs to change with time during the expansion phase, in order to be a fraction of the dynamical timescale, and stay constant thereafter to follow the non-linear evolution accurately in the high-density regions. In our units, with $t_0 = 1$, t is equal to the dynamical timescale, so the following simple functional form is used: $\Delta t = \text{Min}(t\Delta t_0, t^*\Delta t_0)$. This implies that the transition is to be made at $t = t^*$. For all our cluster models we used $t^* = 0.1$.

The choice of softening is discussed extensively in Section 3 and Appendix C. Because the code should mimic a collisionless fluid, a minimum softening length ϵ has to be adopted in order to guarantee this as much as possible. The Plummer force law has its maximum near ϵ , and the maximum scattering will therefore occur around that impact parameter. For such an interaction one can derive

$$\frac{\Delta v}{v} \approx \frac{Gm}{\epsilon v^2} \ . \tag{A1}$$

If one allows a maximal $\frac{\Delta v}{r}$ for individual encounters, the corresponding minimal softening is roughly given by

$$\epsilon_{\min} \approx \frac{Gm}{v^2 \left(\frac{\Delta v}{v}\right)_{\max}}$$
 (A2)

For a given softening parameter (preferably larger than the minimum value just derived), the numerical performance of the code can be controlled by the choice for the basic integration timestep Δt_0 . A guide to this choice is the rootmean-square peculiar velocity v of the particle distribution in combination with the average nearest neighbour distance $r_{\rm nn}$. A criterion could be that an average particle does not move more than a certain fraction f of the average nearest neighbour distance, i.e.

$$\Delta t < f \frac{r_{\rm nn}}{r} \ . \tag{A3}$$

One also would like the particles, when colliding, to trace at least part of each other's density profile, i.e. replacing r_{nn} by the softening parameter ϵ in the above formula if $\epsilon < r_{nn}$. The criterion then becomes

$$\Delta t < f \frac{\min\{r_{\rm nn}, \epsilon\}}{v} \ . \tag{A4}$$

Root-mean-square velocities are listed in Table 2, and the resulting combinations of v and $r_{\rm nn}$ constrain Δt to values also listed in Table 2, for the choice f = 1/4. See Section 3.1 for a discussion of the results.

APPENDIX B: SOFTENED POTENTIALS

In general, an interaction potential is softened if it does not diverge for $r \to 0$, unlike the Kepler potential $\phi(r) \sim 1/r$. The Kepler potential is of course the solution to the Poisson equation for a point mass, so the idea is to convolve the density distribution, a sum of delta functions, by convolving it with a smoothing kernel $W(\mathbf{r}, \epsilon)$:

$$\rho^{W}(\mathbf{r}) = \int W(\mathbf{r} - \mathbf{r}', \epsilon) \rho(\mathbf{r}') d\mathbf{r}'$$
(B1)

(definitions from Hernquist & Barnes 1990). The Plummertype softening

$$W(r,\epsilon) = \frac{3}{4\pi} \frac{\epsilon^2}{(r^2 + \epsilon^2)^{5/2}}$$
 (B2)

transforms point masses (with mass M) into Plummer models (Plummer 1911) with a density profile given by $\rho(r)$ = $MW(\mathbf{r}, \epsilon)$ which has a ('softened') interaction potential

$$\phi(r) = -\frac{GM}{(r^2 + \epsilon^2)^{1/2}} \ . \tag{B3}$$

Another type of softening is 'Hernquist-softening' (Hernquist 1990), using the smoothing kernel

$$W(r,\epsilon') = \frac{1}{2\pi} \frac{\epsilon'}{r(r+\epsilon')^3} , \qquad (B4)$$

which again convolves point masses to mass distributions with density profiles $MW(r, \epsilon')$. The softened potential now is

$$\phi(r) = -\frac{GM}{r + \epsilon'} \,, \tag{B5}$$

which is conveniently simple! We examine some properties of these potentials and their density profiles.

First consider the Plummer model again. For isotropic spherical Plummer models the central velocity dispersion σ_0 is related to the softening parameter:

$$\sigma_0^2 = \frac{GM}{6\epsilon} \ . \tag{B6}$$

The total mass contained within r is

$$M_{\rm Pl}(r) = \frac{M}{(1 + \frac{\epsilon^2}{r^2})^{3/2}} ,$$
 (B7)

which implies a half-mass radius

$$R_{\rm h,Pl} = \frac{\epsilon}{\sqrt{2^{2/3} - 1}} \approx 1.3\epsilon \ . \tag{B8}$$

The surface density profile is obtained by integrating the Plummer density profile along the line of sight, resulting in

$$\mu_{\rm Pl}(R) = \frac{M}{\pi} \frac{\epsilon^2}{(\epsilon^2 + R^2)^2} , \qquad (B9)$$

where R is the radial distance on the sky. The total potential energy U is given by

$$U = -\frac{3\pi}{32} \frac{GM^2}{\epsilon} \ . \tag{B10}$$

The total kinetic energy is given by the virial theorem, i.e. T =-U/2, and the isotropic velocity dispersion $\sigma^2 \equiv 2T/M =$ -U/M is given by

$$\sigma^2 = \frac{3\pi}{32} \frac{GM}{\epsilon} , \qquad (B11)$$

which is roughly twice the central velocity dispersion. Aarseth & Fall (1980) list some more properties of the Plummer model.

326 E. van Kampen

The Hernquist model has a more complicated surface density profile (Hernquist 1990):

$$\mu_{\rm Hq}(R) = \frac{M}{2\pi} \frac{\left[(2\epsilon'^2 + R^2)X(R) - 3\epsilon'^2 \right]}{(\epsilon'^2 - R^2)^2}$$
 (B12)

with
$$X(R) = \begin{cases} \frac{\epsilon' \cosh^{-1}(\epsilon'/R)}{(\epsilon'^2 - R^2)^{1/2}}, & \text{for } 0 \leqslant R \leqslant \epsilon' \\ \frac{\epsilon' \cos^{-1}(\epsilon'/R)}{(R^2 - \epsilon'^2)^{1/2}}, & \text{for } \epsilon' \leqslant R \leqslant \infty \end{cases}$$

This follows from the total mass distribution

$$M_{\rm Hq}(r) = \frac{M}{1 + (\epsilon'/r)^2}$$
 (B13)

with corresponding half-mass radius

$$R_{\rm h,Hg} = (1 + \sqrt{2})\epsilon' \approx 2.41\epsilon'$$
 (B14)

The potential energy now is

$$U = -\frac{GM^2}{6\epsilon'} \tag{B15}$$

and therefore the velocity dispersion

$$\sigma^2 = \frac{GM}{6\epsilon'} \,. \tag{B16}$$

The two softening parameters can be related in several ways. One is to demand that the half-mass radii are equal, which then implies from (B8) and (B14) that

$$\epsilon \approx 1.85\epsilon'$$
 . (B17)

Another option is to match the potential energies (or, equivalently, the gravitational radii, or the kinetic energies, or the velocity dispersions), which gives

$$\epsilon \approx 1.77 \epsilon'$$
 . (B18)

An observation we can make here is that both profiles have

$$R_{\rm h} \approx 0.4 \frac{GM}{\sigma^2} \ , \tag{B19}$$

as is the case for many simple spherical systems (Spitzer 1969). We use this relation as a criterion for whether a group of particles can be considered a galaxy in our simulation.

APPENDIX C: OBSERVED PROFILES VERSUS SOFT PARTICLE PROFILES

The best-fitting profile for observed galaxies is the de Vaucouleurs profile

$$I_{\rm dV}(R) = I_{\rm e} \exp(-7.67[(R/R_{\rm e})^{1/4} - 1])$$
, (C1)

which has I_e and R_e as fitting parameters. Also used is the Hubble-Reynolds profile

$$I_{\rm HR}(R) = I_0 \frac{a^2}{(R+a)^2} ,$$
 (C2)

where I_0 and a are the parameters to be fitted. The shapes of both profiles are fixed: the parameters can only rescale R and I(R) linearly. The same is true for the Plummer profile, where we relate the mass M to a central surface brightness $I_0^{\rm Pl} = M/(4\pi\epsilon^2\Upsilon)$, assuming a constant mass-to-light ratio Υ . For the Hernquist profile $I_{\rm Hq}(R)$ diverges for $R \to 0$, so we should adopt for example $I_\epsilon^{\rm Hq} = I_{\rm Hq}(\epsilon)$ to characterize the amplitude of I(R).

Table C1. Fits for Plummer and Hernquist surface density profiles.

range	fitting	I_0^{Pl}	ϵ	χ ²	$I_{\epsilon}^{ m Hq}$	ϵ'	χ^2	ϵ/ϵ'
[kpc]	profile	$[10^{-9}]$	[kpc]	$[10^3]$	[10 ⁻⁹]	[kpc]	$[10^3]$	
2–15	dV	7.40	7.0	37.9	2.02	6.03	1.1	1.16
	HR	7.22	6.9	49.1	2.06	5.78	3.4	1.19
5-30	dV	2.50	12.3	23.9	1.39	7.36	0.1	1.67
	HR	2.00	13.8	39.1	0.77	10.01	3.4	1.38
10-50	dV	1.00	18.4	13.2	1.40	7.32	0.2	2.51
	HR	0.67	24.1	28.5	-0.30	16.41	2.7	1.46
2-50	dV	4.15	11.1	154.8	1.73	6.68	1.6	1.66
	HR	3.34	13.0	262.5	1.04	9.10	27.6	1.43

Kormendy (1977) found well-fitting intrinsic relations for the parameters of both profiles in a sample of normal galaxies: $I_e = 1.271 \times 10^{-8} R_e^{-1.21}$ and $I_0 = 9.462 \times 10^{-8} a^{-1.17}$. He also found a good relation between the Hubble-Reynolds (HR) and the de Vaucouleurs (dV) profiles in the approximate range a to 20a: $I_0 = 128.23I_e$ and $a = 0.093R_e$. We want to find a similar relation between the soft particle profile parameters and the HR and dV profiles in about the same range. The ellipticals in Kormendy's sample had de Vaucouleurs radii R_e in the range of 1.0 kpc to 14.1 kpc, so we take $R_e = 10$ kpc for a bright cluster elliptical. For other values we can roughly scale the values of ϵ (for the Plummer model) and ϵ' (for the Hernquist model). It will depend on the fitting range in R which softening parameter fits best to the observed profile, so we fitted the Plummer and Hernquist laws to both profiles for a set of fitting ranges. We used non-linear χ^2 fitting to fit log I against $R^{1/4}$. The results are presented in Table C1, where the values for I_e , I_0 and a that were used for the fits are obtained from Kormendy's relations for our choice $R_e = 10$ kpc.

One example is shown in Fig. C1, where all four mentioned profiles are plotted, with the Plummer and Hernquist laws being fits to the de Vaucouleurs law in the range of 5 to 30 kpc (the third row of Table C1). What is gained from the table is the result that a Plummer law does not fit very well over a large range in radius, so one has to compromise on which part of the profile to follow best. The core and the envelope are clearly missing in the Plummer profile for most of the choices. The Hernquist profile fits better, especially for the de Vaucouleurs profile, but note that it was designed to do so (Hernquist 1990)! Plummer softening is most often used because it has a much larger and therefore softer core, which is preferable from a numerical point of view, but it seems that real galaxies are better modelled by the much harder Hernquist profile. Therefore both types of softening are tested at various points in this paper to investigate the difference it makes to the final cluster models.

Finally, the last column of Table C1 reveals that neither softening parameter fits consistently with respect to the other. In general ϵ/ϵ' is smaller than both relations (B17) and (B18) suggest. However, for the best fit (lowest χ^2), being the fit to a de Vaucouleurs profile over a range of 10 to 50 kpc, we find this fraction to be significantly higher. The difficult fitting of the Plummer model is mostly responsible for this behaviour. Therefore both relations (B17) and (B18) are sufficiently accurate for our purposes.

The actual choice for the galaxy particle softening will matter most during encounters, so we should also compare

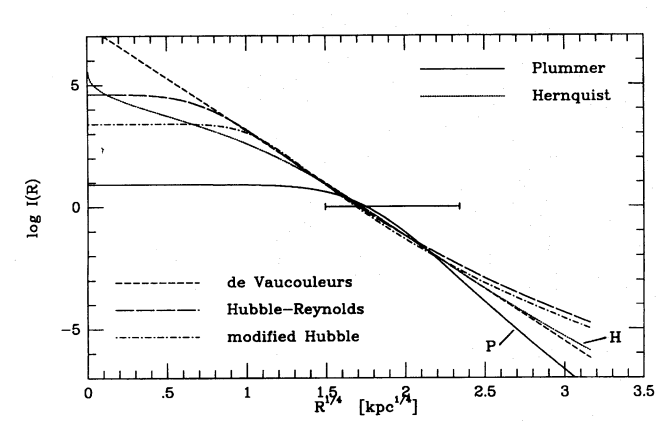


Figure C1. Two theoretical and two observational luminosity profiles for elliptical galaxies. The theoretical Plummer and Hernquist profiles are fitted to a de Vaucouleurs profile over the range 5–30 kpc, as indicated by the horizontal bar. The Hubble-Reynolds profile is shown for comparison.

the soft particle profiles with profiles of interacting galaxies. Two pairs of interacting galaxies imaged by Wright et al. (1990) have profiles that flatten towards the core, which might be better modelled by a Plummer law than by a Hernquist model.

There is much evidence for the existence of a substantial amount of dark matter in galaxies (see for recent reviews for example de Zeeuw 1992; Ashman 1992) which resides in haloes surrounding the luminous part of the galaxy. This could radically change the choice for ϵ as deduced from the relatively well-observed luminous part. The problem is that the distribution of this dark matter is largely unknown. If it follows the luminous matter distribution, ϵ will only increase with the extra mass as $(M_{\text{lum}}/M_{\text{dark}})^{1/3}$. But if the dark matter component distribution is more extended than the luminous one, ϵ will increase even more than that.

We can model spiral galaxies by a spherical model because they are likely to be embedded in a large massive dark halo, which is more or less spherical. For some spiral galaxies, attempts have been made to deduce the shape and total mass of the dark halo from observations. Caldwell & Ostriker (1981) fit for the dark halo of our own Galaxy the following simple spherical profile:

$$\rho_{\rm DH}(r) = \rho_0 \frac{r_{\rm DH}^2}{r^2 + r_{\rm DH}^2} \ . \tag{C3}$$

They find $r_{\rm DH}=7.8$ kpc and $\rho_0=0.014~{\rm M}_{\odot}{\rm pc}^{-3}$, claiming an uncertainty in $\rho(r_{\odot})$ of only a factor of two. This profile falls off much less rapidly for large r than both the Hernquist ($\sim 1/r^4$) and Plummer ($\sim 1/r^5$) laws. However, it is probably truncated at 30 kpc (Little & Tremaine 1987; Carney & Latham 1987), crudely compensating for this. For another typical spiral galaxy, NGC 3198, van Albada et al. (1985) find a similar dark matter profile, with $r_{\rm DH}=12.8$ kpc and $\rho_0=0.0040~{\rm M}_{\odot}{\rm pc}^{-3}$.

Elliptical galaxies lack the gas discs that enable the determination of dark matter profiles: only the region within two de Vaucouleurs radii can reliably be used (de Zeeuw 1992). The mass-to-light ratio in this region is roughly constant, but outside neither constant nor varying mass-to-light ratio profiles can be excluded. However, for giant ellipticals like M87, the brightest cluster elliptical (BCE) of the Virgo cluster, a dark matter profile can be obtained from the X-ray distribution. It is found that $M(r) \sim r$ up to 300 kpc, with a total mass of less than $3 \times 10^{13} \, \mathrm{M}_{\odot}$ (Fabricant & Gorenstein 1983; Stewart et al. 1984). This implies a mass-to-light ratio of about 750 Υ_{\odot} .

The dark halo surface density profiles, found by integrating (C3) along one of the coordinate axes, are much shallower (i.e. 'softer') than any of the luminous profiles:

$$\mu_{\rm DH}(R) = \pi \rho_0 \frac{r_{\rm DH}^2}{(r_{\rm DH}^2 + R^2)^{1/2}}$$
(C4)

If we want to use soft particles as models for galaxies that include dark haloes, the shallowness of the observed dark matter profiles might force us to use a different type of softening (which should still be computationally convenient). But there is also evidence for different halo density profiles for galaxies in clusters as compared to field galaxies (Whitmore, Forbes & Rubin 1988; see, however, Amram et al. 1993 for contrasting evidence). Dark haloes might easily be stripped in clusters, so the choice for the type and amount of softening may still be guided by the luminous matter distribution. We should also take note of the many uncertainties involved in the deductions for $\rho_{\rm DH}(r)$ discussed above.

This paper has been produced using the Royal Astronomical Society/Blackwell Science TEX macros.